Geochemistry Geophysics Geosystems G3

Article
Volume 12, Number 5
17 May 2011
Q05008, doi:10.1029/2010GC003439
ISSN: 1525-2027

Published by AGU and the Geochemical Society

Gravity and seismic study of crustal structure along the Juan de Fuca Ridge axis and across pseudofaults on the ridge flanks

Milena Marjanović and Suzanne M. Carbotte
LDEO, 61 Route 9W, Palisades, New York 10964, USA (milena@ldeo.columbia.edu)

Mladen R. Nedimović
LDEO, 61 Route 9W, Palisades, New York 10964, USA

Also at Dalhousie University, Halifax, Nova Scotia B3H 4J1, Canada

Juan Pablo Canales
WHOI, 360 Woods Hole Road, Woods Hole, Massachusetts 02543, USA

[1] Variations in topography and seismic structure are observed along the Juan de Fuca (JdF) Ridge axis and in the vicinity of pseudofaults on the ridge flanks left by former episodes of ridge propagation. Here we analyze gravity data coregistered with multichannel seismic data from the JdF Ridge and flanks in order to better understand the origin of crustal structure variations in this area. The data were collected along the ridge axis and along three ridge-perpendicular transects at the Endeavor, Northern Symmetric, and Cleft segments. Negative Mantle Bouguer anomalies of −21 to −28 mGal are observed at the axis of the three segments. Thicker crust at the Endeavor and Cleft segments is inferred from seismic data and can account for the small differences in axial gravity anomalies (3–7 mGal). Additional low densities/elevated temperatures within and/or below the axial crust are required to explain the remaining axial MBA low at all segments. Gravity models indicate that the region of low densities is wider beneath the Cleft segment. Gravity models for pseudofaults crossed along the three transects support the presence of thinner and denser crust within the pseudofault zones that we attribute to iron-enriched crust. On the young crust side of the pseudofaults, a 10–20 km wide zone of thicker crust is found. Reflection events interpreted as subcrustal sills underlie the zones of thicker crust and are the presumed source for the iron enrichment.

Components: 11,300 words, 15 figures, 1 table.

Keywords: mid-ocean ridges; propagation; Juan de Fuca Ridge; gravity.

Index Terms: 7220 Seismology: Oceanic crust; 1219 Geodesy and Gravity: Gravity anomalies and Earth structure (0920, 7205, 7240).

Received 18 November 2010; **Revised** 17 March 2011; **Accepted** 25 March 2011; **Published** 17 May 2011.

Marjanović, M., S. M. Carbotte, M. R. Nedimović, and J. P. Canales (2011), Gravity and seismic study of crustal structure along the Juan de Fuca Ridge axis and across pseudofaults on the ridge flanks, *Geochem. Geophys. Geosyst.*, *12*, Q05008, doi:10.1029/2010GC003439.

1. Introduction

[2] Estimates indicate that 15–20% of the total length of the global Mid-Ocean Ridge (MOR) is influenced by the activity of mantle plumes or mantle melt anomalies that are located within ~1000 km from ridge axes [*Ito et al.*, 2003]. The effects of hot spot proximity on MOR are evident

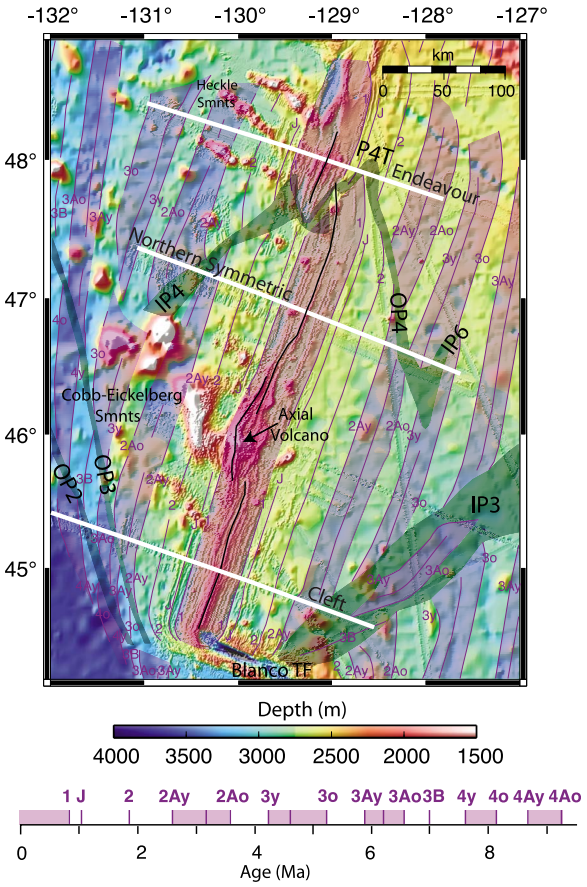

Figure 1. Bathymetry map of the study area with magnetic isochrons superimposed (numbered thin purple lines and light purple shading). Pseudofaults left by former propagating ridge segments are identified from breaks in magnetic isochrons (corresponding age is shown on the bottom scale) and are marked by gray shading (modified from *Wilson* [1993]). Numbering of the pseudofaults is after *Karsten and Delaney* [1989], where OP2, OP3, and OP4 are Outer Pseudofaults 2, 3, and 4, respectively, IP3, IP4, and IP6 refer to Inner Pseudofaults 3, 4, and 6, respectively, and P4T is Propagator 4 Termination at its northern limit. White lines perpendicular to the ridge axis and black lines along the ridge axis show the locations of the seismic and gravity data profiles used in this study.

in elevated ridge axis bathymetry and low mantle Bouguer gravity anomalies [*Ito and Lin*, 1995; *Canales et al.*, 2002; *Eysteinsson and Gunnarsson*, 1995], thickened crust [*Detrick et al.*, 2002; *Darbyshire et al.*, 2000; *Hooft et al.*, 2006] and compositional anomalies [*Schilling et al.*, 1982; *Sinton et al.*, 1983] observed along the ridge axis. At many hot spot influenced ridges, propagation or lengthening of one (propagating) ridge segment at the expense of the adjacent (dying) segment is observed and a causal link between ridge propagation and hot spot proximity has been proposed [*Hey and Vogt*, 1977; *Phipps Morgan and Parmentier*, 1985]. The Juan de Fuca (JdF) Ridge (Figure 1) is a hot spot influenced, intermediate rate spreading center in the northeast Pacific [*Karsten and Delaney*, 1989; *Embley et al.*, 1990; *West et al.*, 2003]. Motion of the Pacific plate over the Cobb hot spot has resulted in the age progressive Cobb-Eickelberg seamount chain which extends ~1800 km from the southern JdF Ridge to the Aleutian trench [*Desonie and Duncan*, 1990]. The Cobb hot spot is believed to currently underlie the axis of the JdF Ridge at the Axial Volcano, a prominent dome-shaped volcanic edifice that rises about 1 km above the surrounding seafloor (summit lies at a depth of 1450 m below the sea level) [*Embley et al.*, 1990; *Chadwick et al.*, 2005]. Bathymetry and magnetic anomaly data indicate that volcanism at the Axial Volcano initiated ~0.5 Ma ago with an ~20 km westward jump of the JdF Ridge axis to override the Cobb hot spot [*Tivey and Johnson*, 1990]. In addition to the prominent Cobb-Eickelberg hot spot chain, numerous small seamounts are present in the region, both as isolated edifices and in small chains, some of which lie close to or intersect the ridge axis. These smaller chains indicate the presence of numerous, shallow, mantle melt anomalies in the region.

[3] Recent observations of crustal structure along the JdF Ridge reveal variations well away from the Axial Volcano, which have been attributed to the influence of the Cobb hot spot and smaller mantle melt anomalies on crustal production at the ridge axis. At the Cleft segment of the JdF Ridge, seismic reflection data reveal Moho two-way travel time (twtt) anomalies that indicate thicker crust (~0.7–1 km) beneath a broad, axis-centered plateau [*Carbotte et al.*, 2008]. Increased crustal production at Cleft for the past 0.5 Ma is inferred, which *Carbotte et al.* [2008] attributed to recent ridge capture of the Cobb hot spot. A similar, axis-centered plateau associated with longer Moho travel times is found at the Endeavor segment. The formation of this plateau is explained by ridge capture of the melt anomaly associated with the Heckle Seamount chain as it is overridden by the ridge axis [*Carbotte et al.*, 2008].

[4] The JdF region has a long history of ridge propagation with 9 major ridge propagating events over the past 18 Ma. These events have been linked to recent changes in JdF plate motion [*Wilson et al.*, 1984; *Wilson*, 1993] and possibly proximity of the

Cobb hot spot [e.g., *Karsten and Delaney*, 1989]. Seismic reflection data collected over the discontinuities on the ridge flanks that mark the former location of propagating ridge offsets (commonly referred to as "pseudofaults," see below), reveal anomalous crustal structure and longer travel times to Moho on the young crust side of these discontinuities [*Calvert et al.*, 1990; *Nedimović et al.*, 2005; *Carbotte et al.*, 2008]. The longer Moho travel times suggest the presence of thicker crust behind propagating ridge tips and that local anomalies in the distribution of melt to the ridge axis may be linked to past events of ridge propagation in this region. However, the crustal velocity information needed to confidently interpret these seismic reflection observations is sparse for the JdF region and Moho travel time anomalies cannot be unambiguously attributed to crustal thickness variations.

[5] In this study, coregistered gravity and seismic reflection data are used to further investigate the nature of these crustal structure anomalies. Two-dimensional forward gravity modeling is conducted with the following primary goals: (1) to assess whether the axial density distributions inferred from gravity data are consistent with thicker crust beneath the Cleft and Endeavor segments, two ridge segments of proposed melt anomaly influence, (2) to assess whether additional anomalous densities (i.e., in the mantle) are required to account for axial gravity anomalies, and (3) to evaluate constraints from gravity data on crustal structure of pseudofault zones and the origin of Moho travel time anomalies observed adjacent to pseudofaults.

[6] With gravity data, crustal thickness variations cannot be uniquely distinguished from variations in crust and/or mantle densities and the common approach is to evaluate a range of plausible models. With a few exceptions, constraints on crustal thickness from seismic studies are not typically available in prior gravity modeling studies of oceanic crustal structure. Here, the available constraints from seismic data for the structure of uppermost crust (layer 2a) and for Moho reflection are used and a suite of models of varying middle-to-lower crustal structure are constructed. We investigate ridge axis structure using models of constant density and thickness crust, constant density and variable thickness crust from the seismic reflection data, varying densities within the crust due to plate cooling away from the ridge axis, and varying densities within the mantle due to plate cooling. Crustal structure at pseudofaults is investigated using best fit models of variable crustal densities given the seismic constraints on crustal thickness. The gravity models support the presence of thicker crust at both Cleft and Endeavor segments and require a broader zone of low densities in the underlying mantle beneath all segments. Preferred models for the ridge flank pseudofaults indicate local zones of thinner and thicker crust and higher densities. The crustal structure models are interpreted in terms of implications for present-day accretion processes along the JdF Ridge and at propagating ridge tips in the past.

2. Regional Setting and Tectonic History

[7] The JdF Ridge is an intermediate rate spreading center with the full spreading rate of 56 mm/yr [*Wilson*, 1993]. It extends for 480 km from the Blanco Transform Fault (TF) in the south to a triple junction in the north (Figure 1). The ridge is composed of seven morphologically distinct segments (West Valley, Endeavor, Northern Symmetric, CoAxial, Axial, Vance and Cleft), separated by second-order nontransform discontinuities. At all segments, a shallow axial graben (50–250 m deep) centered within a <15 km wide axial high, similar to that observed along faster spreading ridges, marks the zone of active magmatism. The width and elevation of the axial high varies along the axis, with the widest axial high at the Cleft and Vance segments (~15 km wide rising 400 m above surrounding seafloor), and the narrowest axial high at the Northern Symmetric and Endeavor segments (5 km wide and 100 m high).

[8] At several of the JdF segments, the axial high is centered on a broader elevated plateau. At the Cleft segment, a 32 km wide plateau bounded by conjugate 300 m high scarps extends along the whole length of the segment, with Moho travel time anomalies relative to older crust suggesting ~1 km thicker crust [*Carbotte et al.*, 2008; *Canales et al.*, 2009]. The age of the plateau estimated from magnetic anomalies is 0.6 Ma, approximately concurrent with westward jump of the JdF Ridge and capture of the Cobb hot spot at ~0.5 Ma. An ~40 km wide axis-centered plateau corresponding to crustal ages of 0.7 Ma is found within the central-southern part of the Endeavor segment and coincides with the on-axis projection of the west flank of the Heckle seamount chain. Moho travel times indicate that this plateau is associated with 0.7–1 km thicker

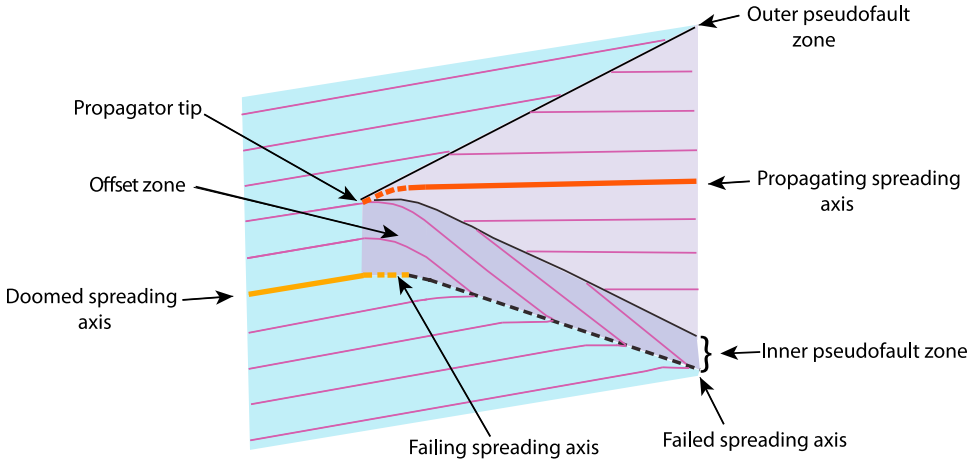

Figure 2. Schematic model of ridge propagation. Tectonic elements of the system are labeled. Normal lithosphere created at the doomed spreading axis is shaded light blue, lithosphere created at the propagating ridge is shaded light violet, and transferred lithosphere is shown in dark violet. Dark purple lines show regularly spaced hypothetical isochrons. V-shaped wake boundaries are delimited with black lines. Propagating ridge segment and dying ridge segment spreading at the full spreading rate are represented by red and orange thick lines, respectively. The active axis with transitional spreading rates and the fossil axis are shown by dashed lines. After *Hey et al.* [1980] and *Kleinrock and Hey* [1989].

crust, which *Carbotte et al.* [2008] attribute to the northwesterly migrating JdF Ridge overriding the mantle melt source for the Heckle seamount chain.

[9] Within our study area, dense magnetic anomaly coverage reveals a complicated history of multiple events of ridge propagation beginning ~18 Ma ago (Figure 1) [*Wilson et al.*, 1984; *Wilson*, 1993]. Ridge propagation involves the migration of one ridge segment across a ridge-axis discontinuity into older crust formed at the neighboring segment, leading to transfer of lithosphere and cessation of spreading along a portion of the adjacent segment [*Hey et al.*, 1980; *Kleinrock and Hey*, 1989] (Figure 2). A V-shaped pair of structural discontinuities, known as the inner and outer pseudofaults, are left on the ridge flanks in the wake of a propagating ridge and are identified from offset magnetic anomalies and disrupted and rotated seafloor fabric. From the V-shaped wakes of offset magnetic anomalies on the flanks of the JdF Ridge, nine episodes of ridge propagation are identified, including three short-lived southward propagators (propagators 5, 6 and 8 in the nomenclature of *Karsten and Delaney* [1989]), three long-lived southward propagators (1, 2, 3) and two long-lived northward propagators (4 and 7). A reversal in the propagation direction of the so-called Cobb offset between the Endeavor and Northern Symmetric segments at ~0.8 Ma was recognized by *Johnson et al.* [1983] which we identify here as the propagator 9.

3. Data Acquisition and Data Description

[10] Multichannel seismic (MCS) reflection and gravity data at the JdF Ridge axis and its flanks were collected during R/V *Maurice Ewing* expedition EW0207 in 2002. The survey included long transects onto the ridge flanks across three of the JdF Ridge segments: Endeavor, Northern Symmetric and Cleft, which are the focus of this study (Figure 1). The total length of each transect is ~300 km, spanning 4–8 Ma old crust, on both sides of the ridge. The survey also included along-axis lines in total length of 450 km extending from the Blanco TF in the south to the northernmost part of the Endeavor segment in the north (Figure 1). Bathymetry data were collected along with the gravity and MCS data, and have been merged with other bathymetric data sets available for the region to form the compilation shown in Figure 1.

[11] Inner pseudofaults are crossed on the Northern Symmetric (IP4 and IP6) and Cleft (IP3) transects along with their conjugate outer pseudofault (at Northern Symmetric OP4, at Cleft OP3 and OP2). The Endeavor transect crosses the northern termi-

nation of Propagator 4 (P4T) at its northern limit before reversal in propagation direction to the south.

3.1. Seismic Data

[12] The MCS data were acquired using a 10 air gun tuned array with a total source volume of 3005 in^3 towed at 7.5 km depth, with shots fired at 37.5 m spacing. For recording, a 6 km long, 480 channel, Syntron digital streamer was used. Detailed description of the data acquisition and processing should be given in earlier papers [*Nedimović et al.*, 2005, 2008; *Canales et al.*, 2005; *Carbotte et al.*, 2008]. From the seismic reflection data, seismic arrivals defining the base of oceanic sediments, the base of seismic layer 2a, the Axial Magma Chamber (AMC), and the Mohorovičić discontinuity (Moho) at the base of oceanic crust (Figure 3a) are identified. Moho is imaged discontinuously beneath the ridge flanks at an average twtt of ~2100 ± 100 ms (~6.6 ± 0.3 km) for all three transects [*Nedimović et al.*, 2005]. Local zones of shorter travel times by 100–200 ms (350–700 m) are found within a number of pseudofaults (Figure 3b). On the young crust side of several pseudofaults, Moho travel times increase of 100–400 ms (350–1300 m) within a 10 km wide region. Within the axial region, Moho is imaged beginning 1–3 km from the ridge axis at each of the segments with differences between segments in Moho twtt within the inner ~20 km. At the Endeavor and Cleft segments, Moho twtts are 200–300 ms (700–1000 m) higher than at Northern Symmetric [*Carbotte et al.*, 2008]. Moreover, the presence of higher twtt to Moho coincides with the plateau regions observed in the bathymetry data at both Cleft and Endeavor (Figure 3b).

3.2. Gravity Data

[13] Gravity data were collected using a Bell Aerospace BGM–3 Marine Gravity Meter System. Positioning and speed of the ship during the survey obtained from the Global Positioning System (GPS) are used to calculate the Eötvös correction. The theoretical gravity reference field (calculated using the 1980 International Gravity Formula) together with the Eötvös correction are subtracted from the observed data to derive the free air anomaly (FAA). Crossover errors calculated for the survey are used to estimate uncertainties in the FAA. The standard deviation of the error distribution is σ = 1 mGal for 213 track crossings (Figure 4). The FAA for all three transects is filtered using a Savitzky-Golay (a least squares) smoothing filter.

[14] As expected, the FAA broadly mimics seafloor bathymetry along each of the profiles with the highest gravity anomaly at the ridge axis and fluctuations on the ridge flanks associated with pseudofaults along with other intermediate wavelength topographic features (Figure 5). The FAA observed at the axis of the Cleft segment is 25 mGal and at Endeavor, 10 mGal. The smallest axial FAA is observed at Northern Symmetric (8 mGal), which is also the deepest segment. An asymmetric high/low FAA pair is associated with the outer pseudofaults with the anomaly low positioned over the old crust side of the pseudofault (Figure 6a). For the Propagator 4 Termination (P4T) crossed by the Endeavor transect, the FAA low is positioned on the young crust side of the pseudofault. The inner pseudofaults are associated with a FAA low roughly centered over the bathymetric depression marking the pseudofault zone (Figures 5 and 6b).

4. Gravity Modeling

[15] As described previously, the primary goals of our study are to use gravity data to further investigate anomalies in crustal structure inferred from seismic reflection data. Two-dimensional forward gravity modeling along the three ridge flank profiles is conducted. The GM-SYS gravity/magnetic modeling software [*Won and Bevis*, 1987], professional basic version is used. The GM-SYS package uses the method of *Talwani et al.* [1959] to calculate the gravitational attraction of two-dimensional bodies of arbitrary shape approximated by an n-sided polygon and constant density. All GM-SYS models are extended to ±30,000 km ("infinity") in the X direction to eliminate edge effects. Uniform structure perpendicular to the profile orientation is assumed with the 2-D approximation. While this assumption is well justified for the ridge axis and flanks where profile orientation is perpendicular to the dominant structural trends, it is less appropriate for the pseudofaults, which are oblique to the profile trend.

[16] In our study, model geometry is defined by crustal layers identified from the seismic data. The simplified lithologic sequence includes the sedimentary cover, the extrusive pillow basalt layer (approximated here as seismic layer 2a), sheeted diabase dikes and gabbros (seismic 2b/3 layer), and

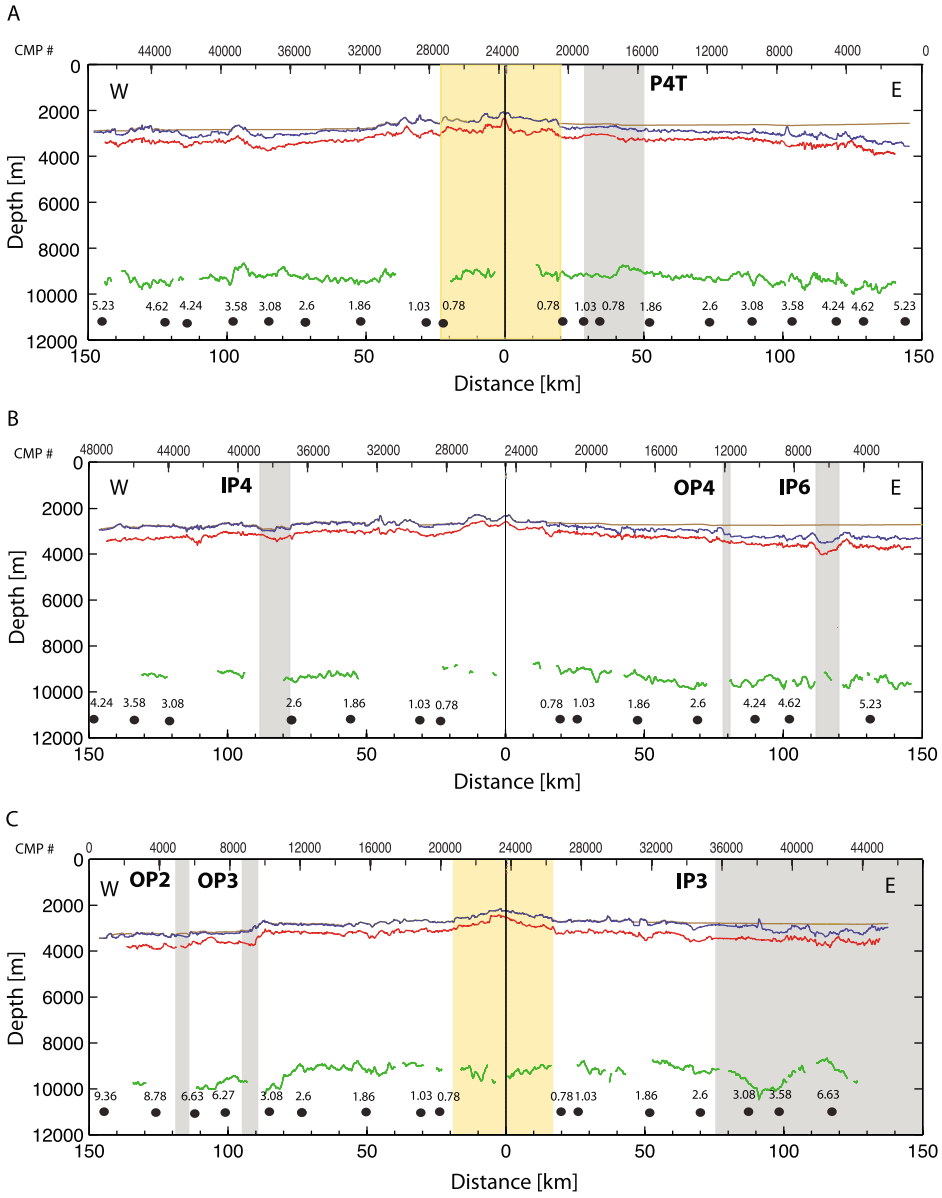

Figure 3a. Interpretation of crustal layers from multichannel seismic (MCS) data for (a) Endeavor, (b) Northern Symmetric, and (c) Cleft transects. Interpreted interfaces include the top of sediments (brown), the top of oceanic crust (blue), the seismic layer 2a/2b boundary (red), and the Moho (green). Gray areas indicate the location of pseudofaults defined from bathymetry; nomenclature for the pseudofaults are the same as in Figure 1. Yellow shaded regions at the Endeavor and Cleft transects mark the extent of the axis-centered plateaus from *Carbotte et al.* [2008]. Crustal ages in Ma from *Wilson* [1993] are indicated along each profile at the bottom with labeled black dots. The horizontal axis is given as distance from the ridge axis in kilometers (bottom) and the common midpoint (CMPs) number (top) along each transect.

upper mantle. All layers are characterized by different seismic velocities and densities.

[17] To set the model geometry, seismic velocity information is needed to convert seismic horizons from measured travel times to depth and an initial model density distribution is established. For seawater and sediments, constant velocities of 1.5 km/s and 1.7 km/s, respectively, are assumed for depth conversion [*Nedimović et al.*, 2005], and constant densities of 1.03 and 1.9 g/cm^3. The prior study of

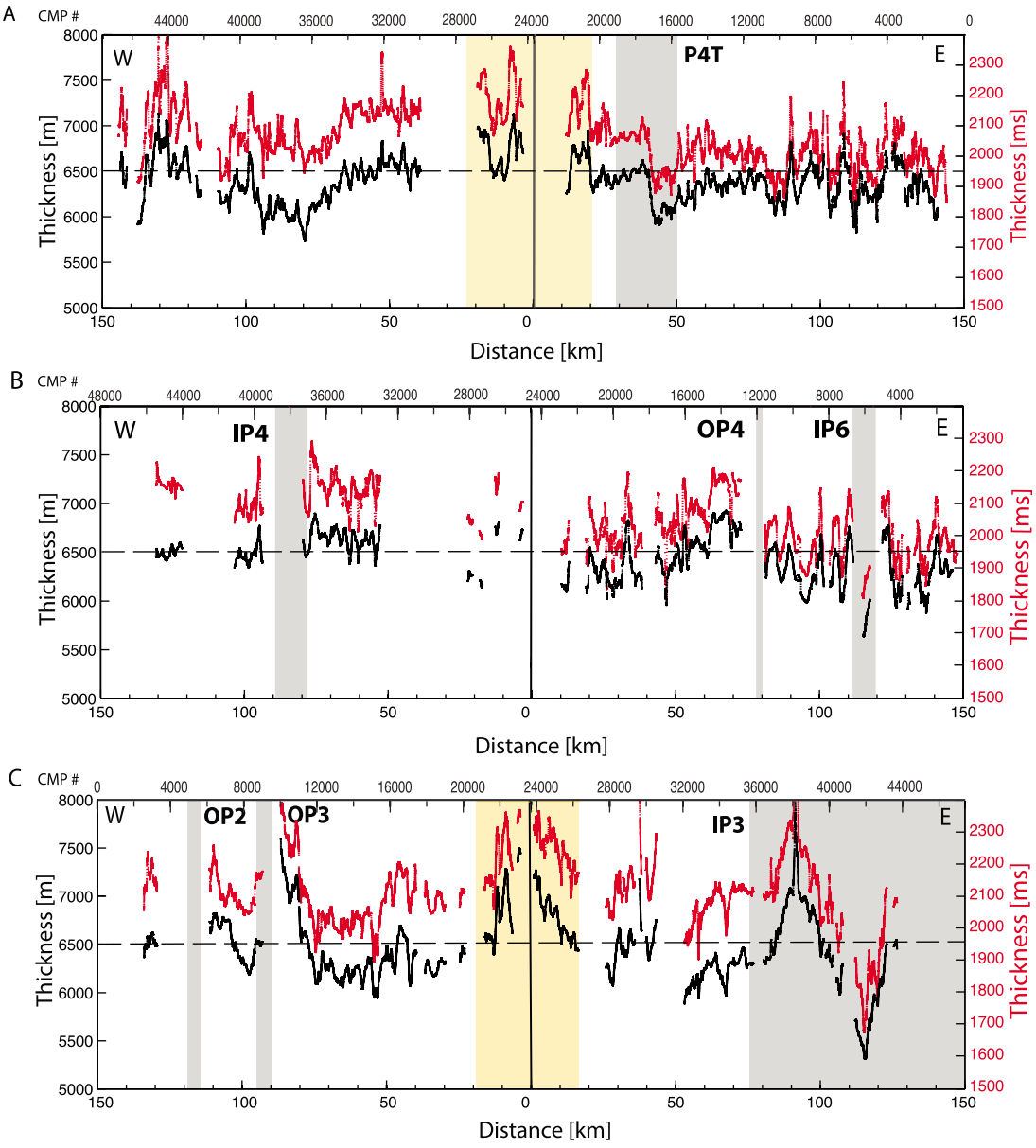

Figure 3b. Thickness of the crust (calculated from top of the oceanic crust to Moho) for (a) Endeavor, (b) Northern Symmetric, and (c) Cleft. Thickness is given as two-way travel time (ms) in red (vertical scale on left) and as thickness (m) (depth converted twtt) in black; depth conversion uses the layer 2a thickness from *Nedimović et al.* [2008] and a constant velocity of 6.67 km/s (Christeson et al., personal communication, 2010). The horizontal axis and shaded rectangles are the same as in Figure 3a.

Nedimović et al. [2008] provides detailed analysis of upper crustal velocities and layer 2a thickness along the three flank transects of our study and is used here to define the geometry and density distribution of layer 2a. For the lower crust, several scenarios for layer geometry and density distribution are tested. Details on the approach for both crustal layers are described below.

4.1. Depth Conversion and Density Distribution for the 2a Layer

[18] For all three transects, the thickness of layer 2a is calculated using seismic velocities and travel times obtained by *Nedimović et al.* [2008] from modeling of common midpoint (CMP) supergathers. Velocities for layer 2a are also used to estimate densities for layer 2a using the empirical

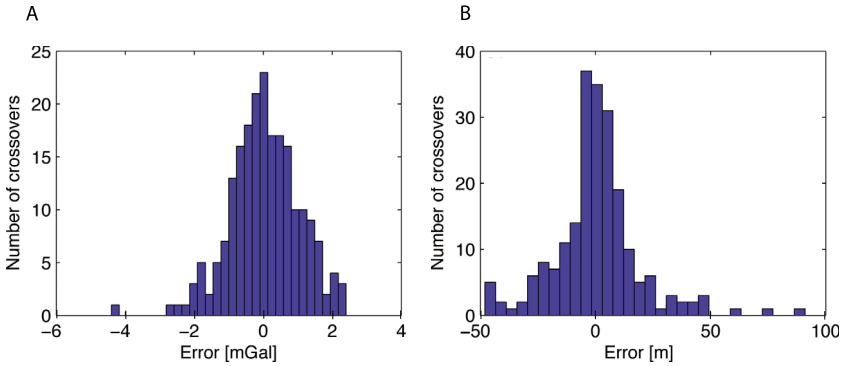

Figure 4. Histograms of crossover errors for (a) observed free-air gravity anomaly, standard deviation for 213 track crossings is σ = 1 mGal, and (b) depth to the seafloor, standard deviation for 213 track crossings is σ = 19 m.

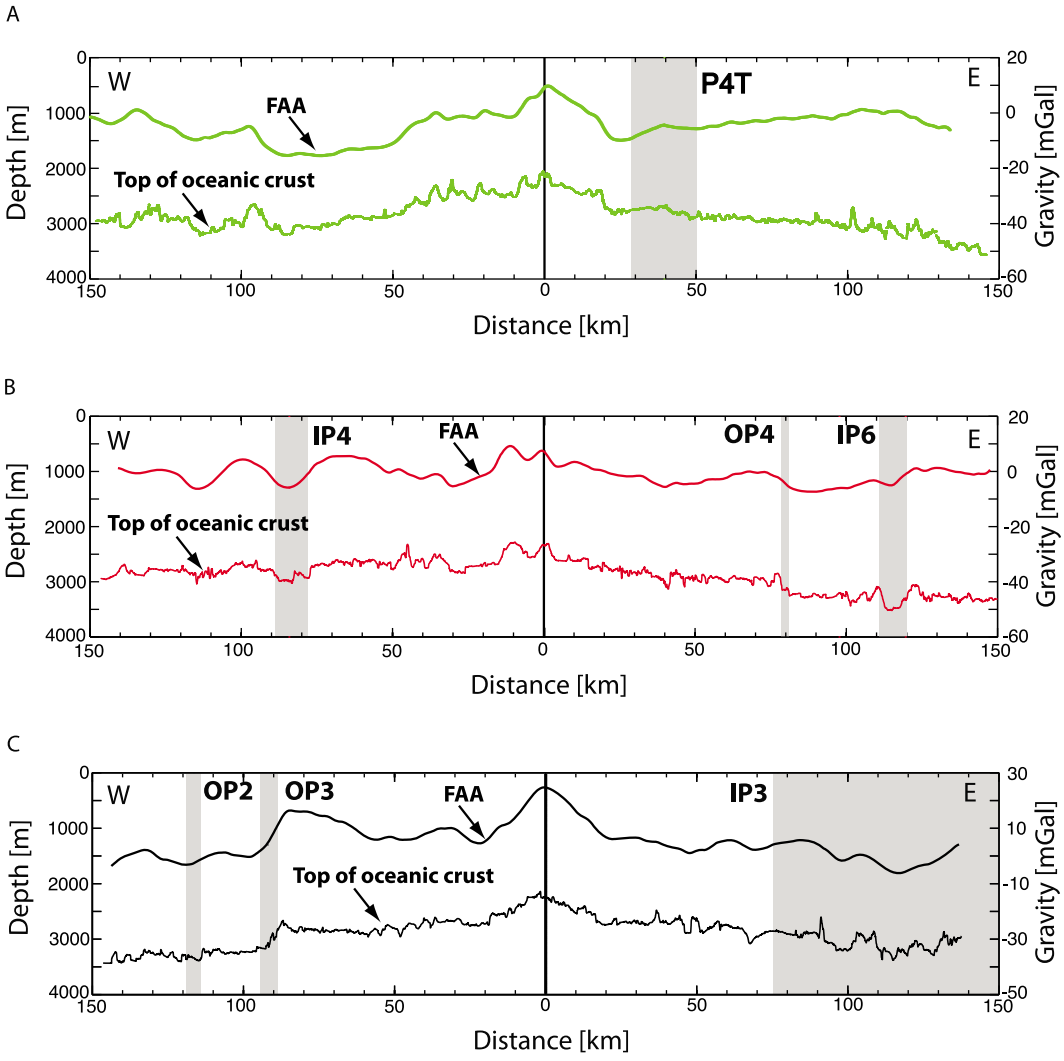

Figure 5. Top of oceanic crust and free-air gravity anomaly (FAA) along the (a) Endeavor (green), (b) Northern Symmetric (red), and (c) Cleft (black) transect (same color code for transects is used in Figures 6, 8, 9b, and 10b). Gray shaded rectangles show the locations of the pseudofaults.

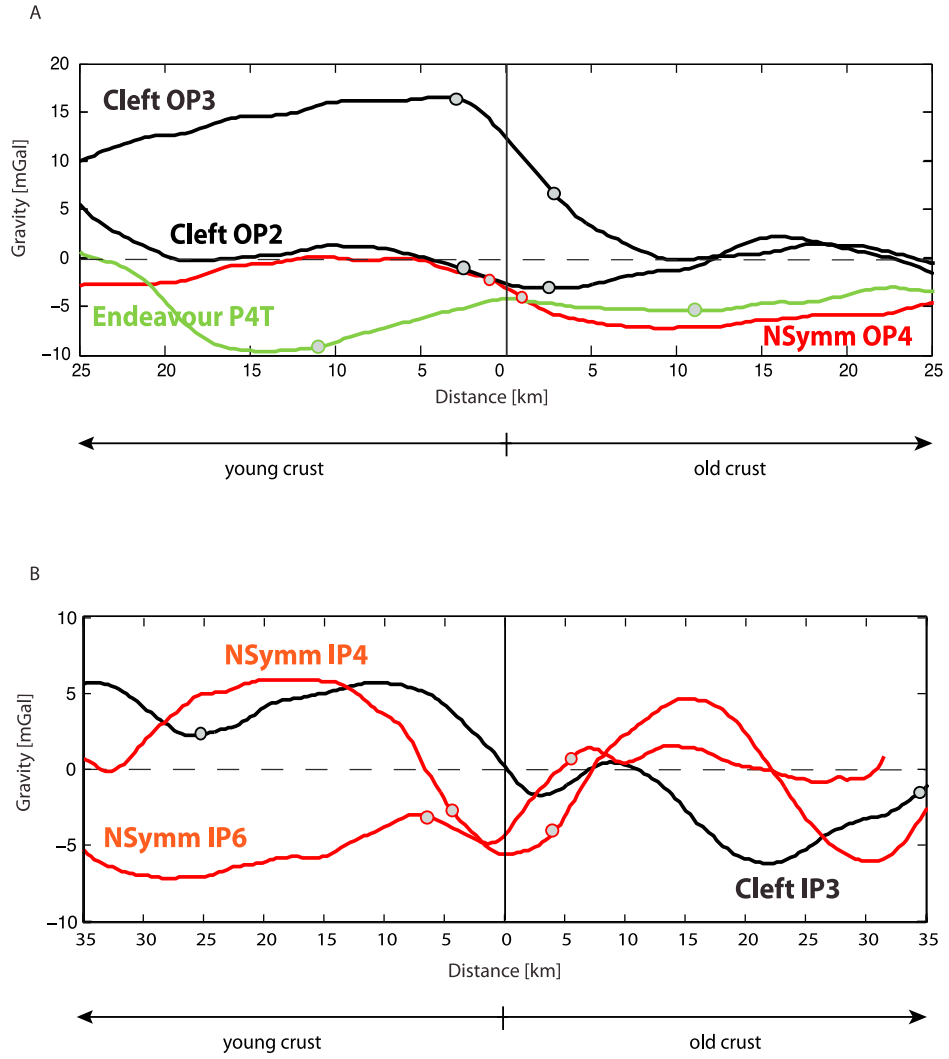

Figure 6. (a) FAA for 50 km sections of each transect centered at the outer pseudofaults. (b) FAA for 70 km sections of each transect centered at the inner pseudofaults. A wider region is shown for the inner pseudofaults due to a much wider IP3 pseudofault zone. Thick vertical black line at 0 km marks the pseudofault centers (except for IP3, for which the zero distance is the midpoint between the western boundary of the pseudofault and the eastern boundary of the rotated block within the propagator wake); the boundaries of each pseudofault estimated from the bathymetry (see text) are indicated with gray circles. All profile crossings are plotted with younger crust side to the left.

relations of *Carlson and Herrick* [1990] derived from analyses of borehole log data of the extrusive basalt layer from DSDP Hole 418A (25°02.10′N, 68°03.44′W). First, porosities are determined according to: $\Phi_f = (-0.35 \pm 0.03) + (2.37 \pm 0.15)S$, where Φ_f is fractional porosity and S is slowness (reciprocal value of velocity from *Nedimović et al.* [2008]). The resulting porosity distribution is then used to define the density distribution from the equation: $\rho_b = 3.0–3.2\Phi_f + 1.2\Phi_f^2$, where ρ_b is bulk density (Figure 7). Based on densities for the uppermost crust derived from on-bottom gravity surveys at the East Pacific Rise [e.g., *Cochran et al.*, 1999] and at the Axial Volcano [*Gilbert et al.*, 2007], we adopt the upper bound densities estimated using the *Carlson and Herrick* [1990] relation (black curve in Figure 7). For modeling purposes the resulting layer 2a density function is approximated by series of constant density blocks. Boundaries for the blocks are chosen to roughly coincide with steps in the calculated density distribution along each transect and average density within the bounded region is assigned to the corresponding block. The calculated densities vary from 1.7 to 2.4 g/cm^3.

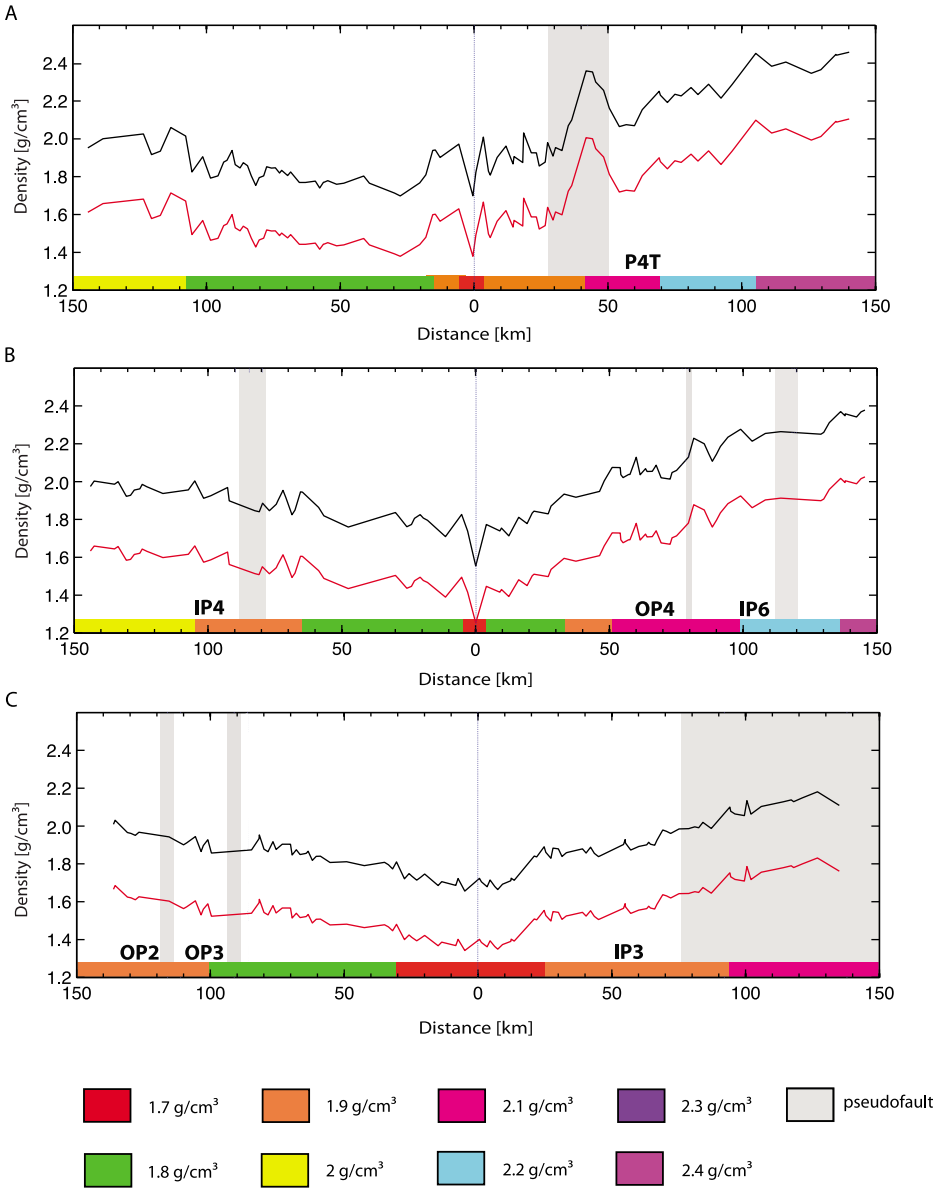

Figure 7. Density distribution for layer 2a along (a) Endeavor, (b) Northern Symmetric, and (c) Cleft transects calculated using porosity-velocity and porosity-density relationships of *Carlson and Herrick* [1990] and seismic velocities for layer 2a from *Nedimović et al.* [2008]. Black and red lines for all three transects correspond with upper and lower bound estimates, respectively; upper bound estimates are chosen here for gravity modeling (see text). For modeling purposes, the resulting variable density function is approximated as a series of constant density blocks shown with a color bar at the bottom of each panel. The gray shaded region shows the location of the pseudofaults.

4.2. Depth Conversion and Density Distribution for Layer 2b/3

[19] To assess the contribution of the thickness of the middle-to-lower crust to the FAA along each transect, velocity constraints for layer 2b/3 are needed. Our long-offset streamer seismic data were evaluated for crustal velocity information using semblance analysis on CMP supergathers in areas of smooth basement. However, high confidence velocity picks were only obtained in a few ridge flank locations (from 6.3 to 7.1 km/s) and no constraints were obtained on velocities within the axial region where Moho twtt anomalies are observed. In the absence of good constraints on crustal velocities along our transects for estimating the thickness of layer 2b/3, gravity modeling was designed to assess both possible thickness and density distributions within this layer, for the axial regions and across the propagator wakes.

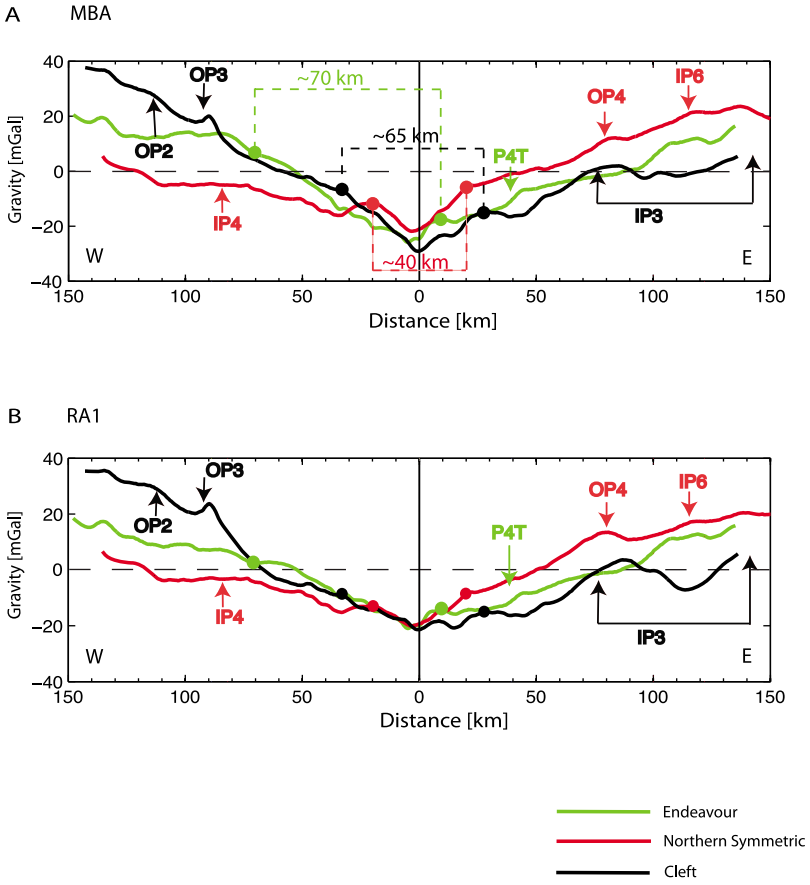

Figure 8. (a) Mantle Bouguer anomaly (MBA) for all three transects calculated by subtracting gravity response of the starting model of constant crustal thickness and density (except layer 2a as given in Figure 7) from observed FAA. The width of the axial MBA low (indicated with colored dots) is defined qualitatively as the distance between inflection points in the long-wavelength (>20 km) anomaly from a high-to-lower gradient. The colored arrows show the locations of the pseudofaults. The arrows correspond with the center of each pseudofault, except for IP3, for which we show its extent. (b) Residual anomaly 1 (RA1) was calculated by subtracting gravity response from the model with the same density distribution as Figure 8a but with seismically inferred crustal thickness (model 1), from the FAA. The arrows and colored dots are as described in Figure 8a.

4.2.1. Modeling Axial Properties

[20] To investigate crustal properties in the axial region, four sets of models were considered. For all models, we use variable density within layer 2a, calculated as described in section 4.1.

[21] The starting model employs constant thickness crust of 6.5 km [e.g., *Wilson*, 1992; *Cormier et al.*, 1995] and constant densities for the water column (ρ_w = 1.03 g/cm^3) and all other layers (sediments ρ_s = 1.9 g/cm^3, middle-to-lower crust ρ_c = 2.75 g/cm^3 and upper mantle ρ_m = 3.3 g/cm^3). The calculated gravity signal from this model is subtracted from the FAA to obtain the Mantle Bouguer anomaly (MBA, Figure 8a).

[22] For model 1, we use constant density crust but variable crustal thickness derived from Moho twtt and an average velocity for the middle-to-lower crust of v = 6.67 km/s, derived from a nearby seismic refraction study (G. L. Christeson et al., personal communication, 2010). All other parameters are as for the starting model. The resulting residual anomaly 1 (RA1) is the gravity signal determined from this model subtracted from the FAA (Figure 8b).

[23] With model 2, we assess the potential contribution of elevated temperatures at the ridge axis associated with crustal accretion. Here, we use a half plate thermal cooling model (taken from *Turcotte and Schubert* [2002]) with the following equation for determining the depth of crustal isotherms:

$$\frac{T_1 - T}{T_1 - T_0} = \mathrm{erfc}\frac{y}{2\sqrt{kx/u}}$$

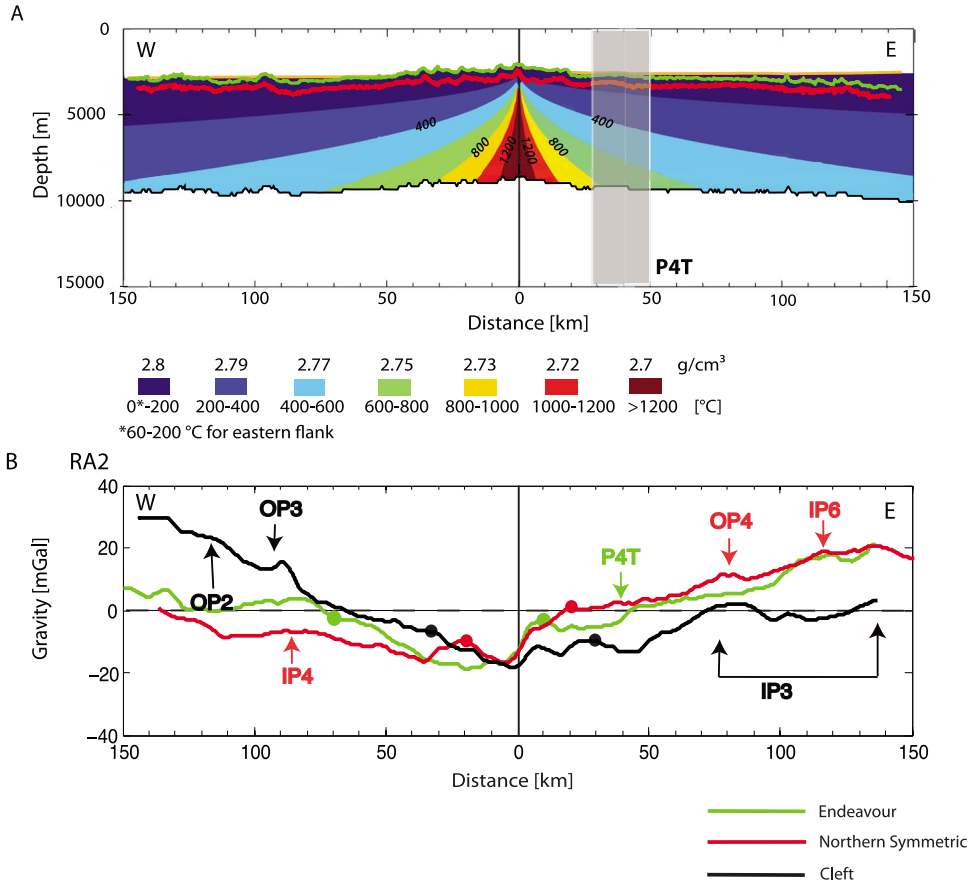

Figure 9. (a) Variable density model assuming half plate thermal cooling (model 2). In this example, calculated isotherms are shown for the Endeavor transect, with the corresponding density distribution estimated from $d\rho = -\rho_0 \alpha_v dT$ as indicated with the color-coded polygons. Variable densities are confined to crust with a constant density mantle below (ρ_m = 3.3 g/cm^3). The depth to sediment-water interface (yellow line), the top of oceanic crust (green line), and the layer 2a/2b boundary (red line) are from seismic data (see text). The depth to crust-mantle boundary (black line) is calculated assuming a constant thickness crust of 6.5 km. Gray shading shows the location of the pseudofault crossing P4T. Model accounts for thermal effects of sediments, which blanket eastern flank of ridge (hereafter referred to as asymmetric thermal model). (b) Residual anomaly 2 (RA2) calculated from model 2 for all transects.

where T_1 initial temperature of half-space (here $T_1 \approx 1200$°C), T_0 temperature at the seafloor (T_0 = 0°C), x distance from the ridge axis, y depth, κ thermal diffusivity (here 1 mm^2/s, taken from Turcotte and Schubert), u half-spreading rate.

[24] Minor modifications to this model are made to account for the thermal effects of the thick sediment cover, which blankets the eastern flank of the JdF Ridge and is expected to thermally insulate the underlying igneous crust. Temperature measurements from ODP boreholes at the base of the sedimentary cover on the east flank of the Endeavor segment are ~60°C [*Davis et al.*, 1997], which we use as T_0 in the equation above to calculate the asymmetric thermal cooling model (Figure 9a). This model is used to define density variations within the middle-to-lower crust at temperature steps (dT) of 200°C using equation $d\rho = -\rho_0 \alpha_v dT$ (where ρ_0, starting density, is 2.7 g/cm^3, and α_v, volumetric coefficient of thermal expansion, is 3 × 10^{-5} K^{-1}, [*Turcotte and Schubert*, 2002]). For the eastern flank of the JdF Ridge, calculated gravity values using this asymmetric thermal cooling model 2 (Figure 9b) differ by up to 8 mGal from gravity models that do not include the thermally insulating effects of the local sediment cover.

[25] In model 3, we calculate the effects of variable densities within the upper mantle as well as within the crust due to half-space cooling (Figure 10a). The mantle density distribution is determined using the same formula as for the crust ($d\rho = -\rho_0 \alpha_v dT$) with starting density, ρ_0 = 3.2 g/cm^3. Calculated

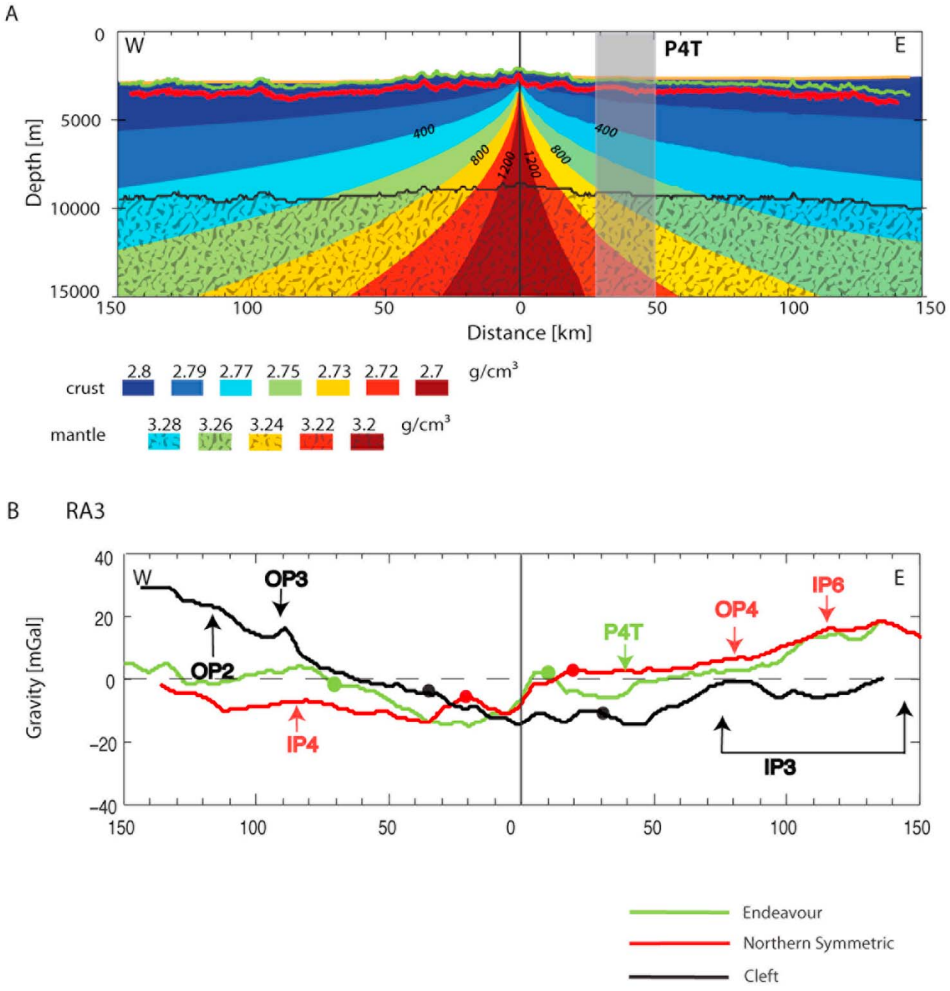

Figure 10. (a) Asymmetric thermal model with variable densities due to half plate cooling (defined as for Figure 9a) for both crust and upper mantle (model 3) shown here for Endeavour transect. The density distribution is indicated by color-coded polygons (upper mantle shown with shaded pattern polygons). (b) Residual anomaly 3 (RA3) for all transects calculated by subtracting gravity signal of model 3 from FAA.

gravity from model 3 subtracted from the observed FAA gives residual anomaly 3 (RA3, Figure 10b).

4.2.2. Modeling Pseudofault Zones

[26] Pseudofault zones are identified on the ridge flanks from offsets in magnetic isochrons (Figure 1) and local disruptions in seafloor bathymetry, with 200–400 m deep troughs at the inner pseudofaults and steps in bathymetry (deeper seafloor on the older plate side) at outer pseudofaults (Figures 3a and 3b). To model gravity anomalies associated with the pseudofault zones, we adopt model 1 of constant crustal density but seismically inferred crustal thickness as the starting model. Pseudofaults are located beyond the expected region of most rapidly varying densities in the upper mantle due to plate cooling (Figures 3a, 3b, and 10b) and we adopt uniform density for the upper mantle. From the starting model, densities within vertical crustal blocks coincident with the pseudofaults and adjoining crust are varied until a good match between calculated and observed gravity signal over the pseudofaults is obtained (Figures 11 and 12). The width of the bathymetric anomalies and zone of disturbed magnetic anomalies are used to set the width of model pseudofault zones, which varies from ~3 km for OP4 at Northern Symmetric transect to ~55 km for IP3 at Cleft transect. Coherent, obliquely trending magnetic anomalies are identified within IP3, indicating the presence of rotated crustal blocks within this inner pseudofault (Figure 1). To examine the possibility that crustal thickness variations could account for the gravity anomalies over the pseudofaults, we also ran models where the thickness of constant den-

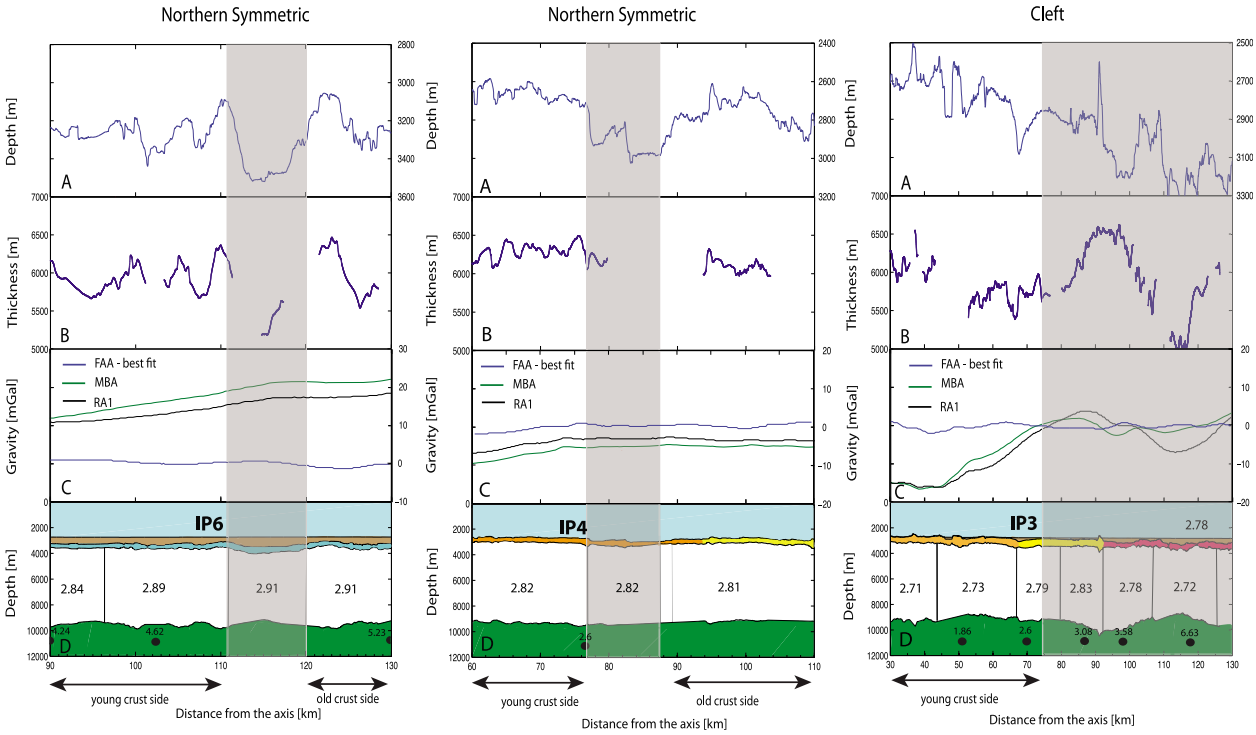

Figure 11. Gravity models for inner pseudofaults crossed along the Northern Symmetric (IP6 and IP4) and Cleft transects (IP3). For each pseudofault crossing we show, from top to bottom: (a) Top of oceanic crust with location of pseudofaults defined from topographic troughs and zone of offset magnetic anomalies in gray shading. (b) Thickness of layer 2b/3 inferred from Moho twtt and constant velocity v = 6.67 km/s (Christeson et al., personal communication, 2010). (c) Gravity model results with Mantle Bouguer anomalies (MBA) from Figure 8a in green line, residual anomaly (RA1) from Figure 8b in black line, and residual anomaly shown in blue line obtained from the best fit model subtracted from observed FAA. (d) Best fit model assuming seismically inferred crustal thickness. The density distribution is as follows: for layer 2A from Figure 7, water column ρ_w = 1.03 g/cm^3 (light blue), sediments (brown) ρ_s = 1.9 g/cm^3, upper mantle (green) ρ_m = 3.3 g/cm^3, final best fit density distribution for middle-to-lower crust is shown with numbered polygons. The crustal ages from magnetic isochrons are shown in Ma and indicated with black dots. Double-sided arrows at the bottom of Figure 11 indicate the younger and older crust side of the pseudofaults.

sity crust is varied until a satisfactory fit between the calculated and observed data is reached.

5. Results

5.1. Axial Region

[27] The MBA along all three transects is characterized by a broad axial low centered at the ridge axis which differs in magnitude and width at the three transects (Figure 8a). Lower axial MBA are observed at the Cleft and Endeavor segments (−28 and −25 mGal, respectively), compared with the Northern Symmetric segment (−21 mGal). The width of the axial MBA low, defined qualitatively by change in slope of the MBA from high to low gradient, is narrower (~40 km) at Northern Symmetric than at Cleft or Endeavor (~70 km).

[28] The differences between transects in the axial MBA are largely account for model 1 of constant crustal density and seismically inferred crustal thickness (Figure 8b). At the ridge axis, residual gravity values are −20 ± 1 mGal, at all three transects. This result supports the inference from the Moho twtt anomalies, of thicker crust within the axial region at the Cleft and Endeavor segments.

[29] The remaining axial anomaly in RA1 requires additional sources of low densities in the axial region at all three segments. Model 2 (RA2) tests the contribution of lower densities in the axial region due to elevated temperatures in the middle-to-lower crust (Figure 9a). This model accounts for 48% of the axial MBA at the Endeavor segment and 38–39% at Cleft and Northern Symmetric (Figure 9b and Table 1). With the addition of lower densities in the upper mantle due to half plate

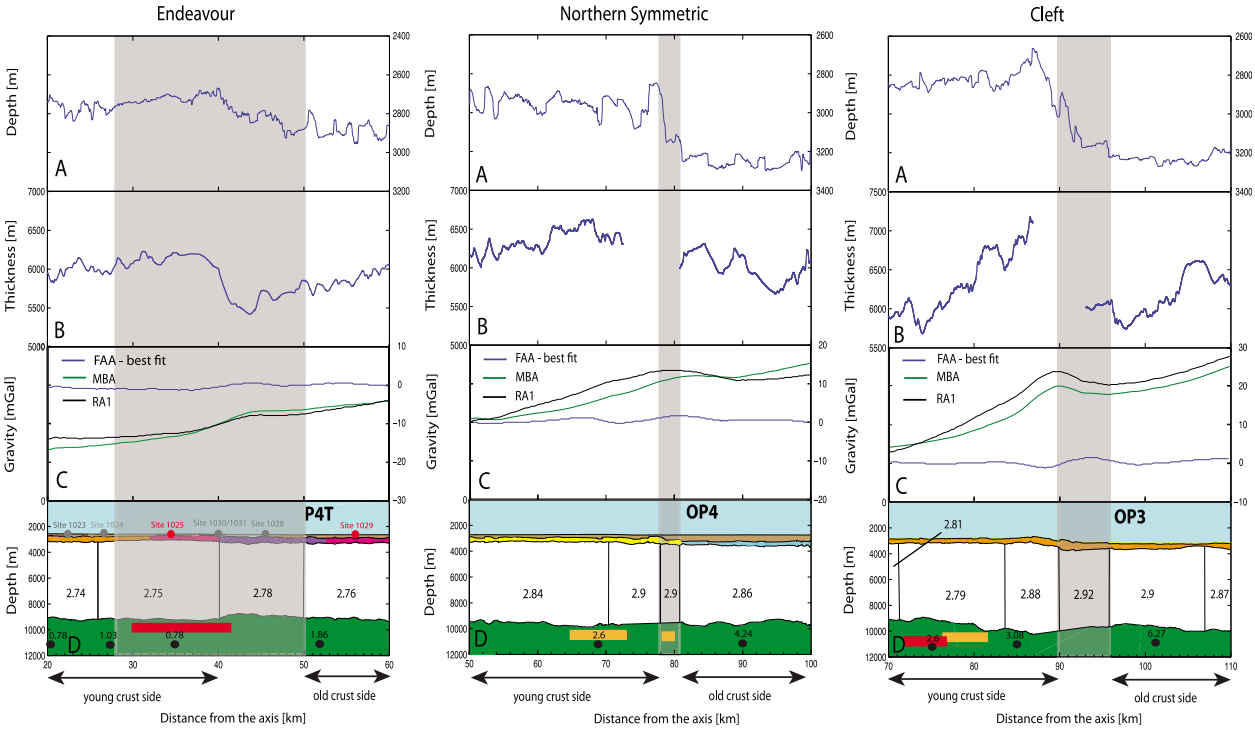

Figure 12. Gravity models for outer pseudofaults crossed along Northern Symmetric (OP4) and Cleft (OP3) transects and the pseudofault termination crossed along the Endeavor transect (P4T). The locations of ODP drill hole sites along the Endeavor profile are indicated (numbered dots); drill holes where FeTi enriched basalts are sampled are indicated in red. The location of sub-Moho reflections in seismic sections interpreted as frozen sills [*Nedimović et al.*, 2005] are indicated with rectangles at the base of the crust (high-amplitude reflections are in red, weak reflections are in orange); vertical size of rectangles is not to scale. All other annotations are as in Figure 11.

cooling (Figure 10a), the calculated anomalies (RA3) account for ~50–76% of the MBA (Figure 10b and Table 1).

[30] At the edge of the axial anomaly, residual anomalies calculated for the half plate cooling models (RA2, RA3) are reduced to near zero on the eastern flank of the Endeavor and Northern Symmetric segments, whereas a broad anomaly low remains on the western flank at both segments. At the Cleft segment, low residual anomalies persist on both flanks, roughly symmetric about the axis (Figures 9b and 10b).

5.2. Propagator Pseudofaults

[31] Along all three transects, the gravity signal from constant thickness and density crust (i.e., the MBA) is inadequate to explain the observed gravity anomalies over the pseudofaults (Figures 11c and 12c) and variations in crustal thickness and/or density are required to fully account for the FAA. At the two inner pseudofaults crossed along the Northern Symmetric transect, thinner crust within the pseudofault zones inferred from the seismic data (~350–700 m), with little variation in density (<0.02 g/cm^3) are sufficient to explain the observed gravity signal (Figures 11c and 11d). Significant variations in density are only needed at the broad inner pseudofault IP3 crossed along the Cleft transect, where crustal blocks of higher density than adjoining crust are required. These higher density blocks correlate with a region of thicker crust inferred from Moho travel times, and rotated

Table 1. Gravity Anomaly Values at the Ridge Axis Calculated From Each Model Along All Three Transects[a]

Segment	MBA (mGal)	RA1 (mGal)	*% MBA*	RA2 (mGal)	*% MBA*	RA3 (mGal)	*% MBA*
Cleft	−28	−21	*25*	−17	*39*	−14	*50*
NSymm	−21	−20	*5*	−13	*38*	−8	*62*
Endeavour	−25	−20	*20*	−13	*48*	−6	*76*

[a]Columns with italicized data indicate the percentage of MBA accounted for by each residual anomaly (calculated as (RA-MBA)/MBA).

crust as inferred from magnetic isochrons. Local zones of sheared and fractured crust presumably accompany this crustal rotation, and crustal velocities may be lower than assumed.

[32] At the outer pseudofaults, variable crustal thickness inferred from the seismic data does not fully account for the gravity anomalies and variable densities are also needed (Figure 12). Best fit models require a zone of higher densities (0.02–0.14 g/cm^3) within all outer pseudofaults compared with the adjacent crust. Moreover, seismic data indicate locally thicker crust (0.35–1.3 km) on the young crust side of the pseudofaults and best fit models require slightly higher density crust extending part way into the younger crust zones. These young, thick crust regions are located beyond the zone of possible reduced crustal velocity caused by enhanced crustal shearing and fracturing in the pseudofault and hence overestimated crustal thicknesses are not expected. In all cases, higher density crust is inferred on the old crust side of the pseudofaults compared with the young crust side, which is consistent with an age contrast across the discontinuity (Figure 12d).

[33] Given the uncertainties in crustal thicknesses, due to both the lack of detailed crustal velocity information and intermittent Moho imaging, we also determine models of constant density crust but variable crustal thickness that give the best fit to the FAA. The results show that much thinner crust (by ~1.8 km for total crustal thickness of ~4.7 km) within the outer pseudofaults would be needed. To match the observed travel times to Moho for this crustal thickness, very slow seismic velocities (4.5 km/s) would be required to extend throughout the middle-to-lower crust. Evidence for such low seismic velocities are found only in the upper crust even at fracture zones [e.g., *Van Avendonk et al.*, 1998] and we favor a model of higher density and moderately thinner crust (~0.5 km) within the outer pseudofaults as the more plausible source of the observed gravity anomalies.

6. Along-Axis Models and Comparison With Earlier Study

[34] *Hooft and Detrick* [1995] conducted 2-D forward gravity modeling along the JdF Ridge axis using data available at the time from the historical archives of the National Geophysical Data Center (NGDC). In conflict with our results from the ridge-perpendicular transects, their analysis indicated comparable crustal thickness and/or mantle densities beneath the Cleft and Northern Symmetric segments (their Figure 5). To better understand the origin of the discrepancy with our results, we modeled along-axis gravity data collected during our EW0207 survey using the same model parameters as *Hooft and Detrick* [1995] (Figure 13): constant crustal thickness $d = 6$ km, constant density for seawater $\rho_w = 1.03$ g/cm^3, crust $\rho_c = 2.7$ g/cm^3 and upper mantle $\rho_m = 3.3$ g/cm^3. With the exception of the Axial Volcano and the north end of Northern Symmetric, the along-axis MBA defined by these model parameters (Figure 13c, green line), accounts for the observed along-axis gravity signal. Furthermore, the MBA indicates little difference in axial density structure at the Northern Symmetric and Cleft segments, which is consistent with the results of *Hooft and Detrick* [1995], but contradictory to the results from our study at the ridge-perpendicular transects (Figure 8a). We attribute this discrepancy to the inherent limitations of the 2-D assumption for an along-axis geometry. Uniform seafloor depths and crustal structure perpendicular to the ridge are assumed in the 2-D model geometry, which are clearly invalid assumptions given the pronounced axial high topography and rapid subsidence of the crust, along with presence of local near axis seamounts. These results highlight the limitations of 2-D along-axis gravity studies of along-axis profiles and the need for caution in interpretation of the resulting along-axis MBA.

[35] To facilitate direct comparison between the axial MBA from our study with *Hooft and Detrick* [1995], we recalculate the FAA anomaly from our study (Figure 13b, green line) using the 1967 Gravity International Formula (IGF) used in the earlier study (Figure 13b, red line). Even after accounting for the differences due to the gravity reference field used, the observed axial gravity anomaly for these two studies differ. The FAA from the *Hooft and Detrick* [1995] study show short wavelength variations that are not present in the modern data as well as significantly lower values (up to 25 mGal) from the Axial segment up to the southern end of the Endeavor segment (Figure 13b). Discrepancies are also observed in the bathymetry data with deeper seafloor depths for much of the ridge axis in the Hooft and Detrick profile (Figure 13a). We attribute these differences to a poorly sampled and mislocated ridge axis in the earlier study due to the sparse gravity data coverage and large navigation uncertainties associated with the largely pre-GPS data available. These differences in the observed FAA and seafloor depth for

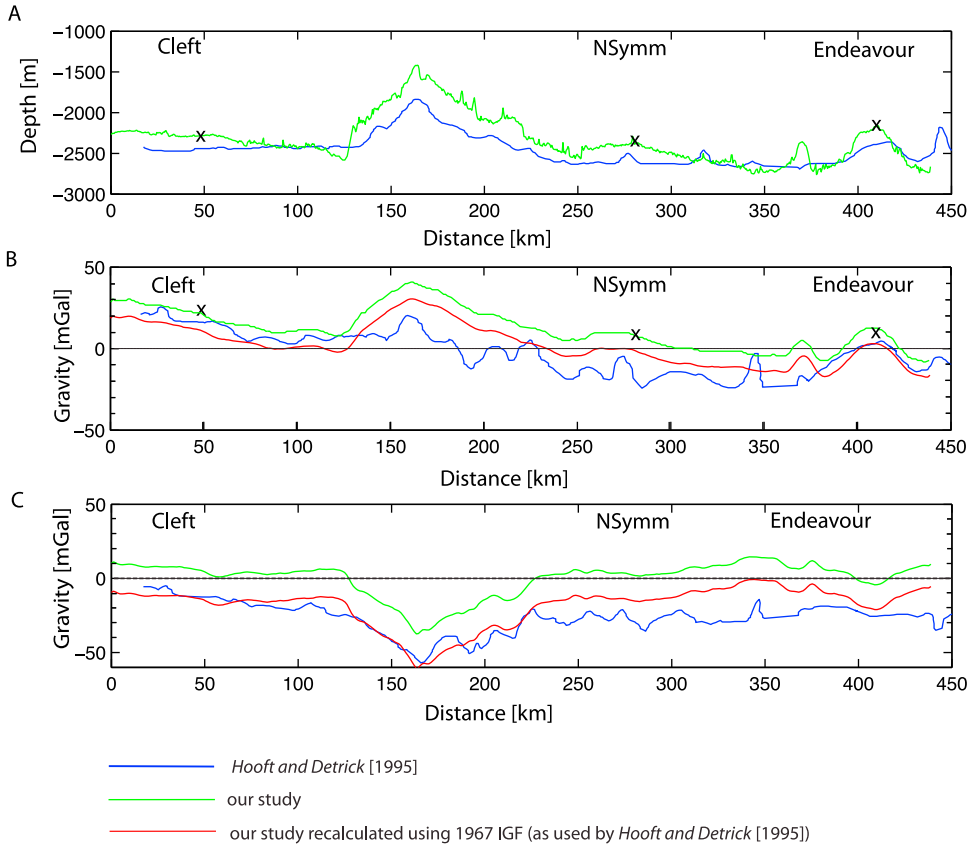

Figure 13. Comparison of along-axis data with earlier study of *Hooft and Detrick* [1995]. (a) Along-axis bathymetry data from our study are in green and from *Hooft and Detrick* [1995] are in blue. The horizontal axis is the distance in kilometers calculated from the origin at 44°35.688′N and 130°23.6639′W. (b) FAA from *Hooft and Detrick* [1995] in blue. FAA obtained from our study using the Potsdam International Gravity Formula (IGF) from 1980 in green and recalculated using 1967 IGF shown in red (see text). (c) Mantle Bouguer anomaly (MBA) obtained by subtracting calculated gravity for constant thickness and density crust (see text) from FAA. MBA from Hooft and Detrick in blue, from our study in green and from our study recalculated using 1967 IGF in red. Cross symbols ("X") show the seafloor depth (Figure 13a) and the FAA anomaly (Figure 13b) recorded at the three cross-axis lines.

the two studies account for the discrepancies in calculated along-axis MBA values (Figure 13c).

7. Discussion

7.1. Variations in Axial Structure

[36] Modeling results indicate that the differences in axial gravity anomalies at the Cleft, Endeavor and Northern Symmetric segments can be explained by the differences in crustal thickness obtained from the reflection data (Figure 8b), with thicker crust in the near axis region at Cleft and Endeavor. The modeling results also indicate that thermally reduced densities in the crust and upper mantle, expected in the axial region due to elevated temperatures, only account for part of the remaining MBA (76% at the Endeavor segment to 50% at the Cleft segment, Figure 10b and Table 1). The remaining anomaly requires the presence of additional low densities at all three segments, presumably related to the presence of melt. These results are similar to those obtained in the earlier study of *Wilson* [1992] from gravity modeling of a composite cross-axis profile for the Cleft segment, where he found that reduced densities due to thermal expansion within the crust and upper mantle account for 60% of the axial MBA. *Wilson* [1992] attributed the remaining anomaly to an additional lower density body that extends 20 km into the upper mantle and that corresponds to ~3% melt.

[37] After accounting for thermally reduced densities, axial gravity models reveal residual anomaly lows that are markedly asymmetric about the axis

of the Northern Symmetric and Endeavor segments, with broad lows extending beneath the western flank of the ridge (Figures 9b and 10b). As noted earlier, the JdF region is characterized by numerous near-axis seamounts, predominantly found on the Pacific flank of the ridge. *Davis and Karsten* [1986] attribute this asymmetric distribution to small upper mantle melt anomalies that are tapped by the northwesterly advancing JdF Ridge. The asymmetric gravity anomalies at the Endeavor and Northern Symmetric transects suggest warmer temperatures or presence of higher percent of melt beneath the Pacific plate, consistent with the inference of *Davis and Karsten* [1986].

[38] In contrast to the Endeavor and Northern Symmetric transects, the residual gravity anomaly low extends beneath both flanks of the Cleft segment, and is more pronounced on the eastern flank, persisting up to 70 km to the east of the axis. Regional scale south-to-north gradients in a number of properties along the JdF Ridge, including axial depth and presence and depth of the midcrust magma lens, indicate a warmer axial regime at the Cleft segment than elsewhere along the JdF Ridge (with the exception of the Axial Volcano [*Carbotte et al.*, 2006]). Furthermore, within the Cleft segment, the shallowest magma lens and thickest crust [*Canales et al.*, 2009] is found at the southern end of this segment adjacent to the Blanco TF, in spite of the large age offset and expected cold edge effect associated with this transform fault. *Carbotte et al.* [2008] attribute enhanced magma supply/thicker crust at the Cleft segment to damming of southward directed subaxial, asthenospheric flow from Cobb by the Blanco TF. Interestingly, *Gregg et al.* [2007] in their analysis of fast and intermediate rate transform faults, find a pronounced MBA low associated with the Blanco TF, with the largest density deficit located along the northwesterly portion that is closest to the Cleft segment. The origin of these low densities within the transform domain is presumably also linked to the low-density mantle inferred from our data beneath the east flank of the Cleft segment (located ~50 km to the north from the Blanco TF).

7.2. Crustal Structure of Pseudofault Zones

[39] Modeling of gravity and seismic data from the pseudofault zones indicates the presence of thinner and/or denser crust within these discontinuities. Evidence for thinner crust within pseudofaults is seen elsewhere [*West et al.*, 1999; *Kruse et al.*, 2000] and is attributed to low melt supply at propagating ridge tips as spreading rate gradually decreases from full rates to zero behind the tip [*Hey et al.*, 1992; *West et al.*, 1999; *Kruse et al.*, 2000]. Extensive shearing and rotation of preexisting crust is expected between propagating and dying ridge segments (Figure 2), and could also contribute to thinner crust [*Kleinrock and Hey*, 1989; *Martinez et al.*, 1991; *Hooft et al.*, 1995]. Our best fit models show that crust is on the order of 0.5 km thinner within the inner pseudofaults compared with adjacent crust. Even greater crustal thinning (by ~1.8 km for total crustal thickness of ~4.7 km) is required to fully account for the gravity anomaly at the outer pseudofaults assuming constant crustal densities. However, to match the measured Moho twtts at the pseudofaults for this crustal thickness, seismic velocities of ~4.5 km/s would be required throughout the middle-to-lower crust, which is much slower than average crustal velocities observed at fracture zones, and we consider such low velocities unlikely. Instead, we favor the presence of a local zone of higher density crust within the outer pseudofaults.

[40] Higher density crust is consistent with the presence of FeTi basalts that are commonly sampled at modern propagating ridges [*Hey et al.*, 1992; *Carbotte and Macdonald*, 1992; *Klein et al.*, 1991). In the JdF region, FeTi basalts are sampled along the ridge axis at the intersection of Cleft segment with the Blanco TF and at the northern end of the Northern Symmetric segment. In both locations the compositions were attributed to ridge propagation [*Sinton et al.*, 1983]. ODP drilling along the Endeavor FlankFlux transect, which is coincident with our profile, sampled fractured ferrobasalts at two sites on the ridge flanks (1025 and 1029, Figure 12d, Endeavor) located nearby the propagator wake PT4 [*Davis et al.*, 1997; *Marescotti et al.*, 2000]. Our calculations indicate that a 2.5–3 km thick layer of FeTi basalts assuming a density of ~3.1–3.2 g/cm^3 [from *Karato and Becker*, 1983; *Iturrino et al.*, 1991] and no variation in crustal thickness, would completely account for the observed FAA over the outer pseudofaults (with the rest of the crust at constant density). However, iron enrichment is also expected to be associated with slower seismic compressional wave velocities of ~5.5 km/s [e.g., *Iturrino et al.*, 1991], which can explain only up to 850 m thinning of the crust. Based on these results and the presence of FeTi basalts near the pseudofault zone at Endeavor, we favor contributions from both higher density iron enriched crustal rocks and moderately thinner crust (equivalent to the thinning at the inner pseudofaults) to account for the gravity anomalies associated with the outer pseudofaults.

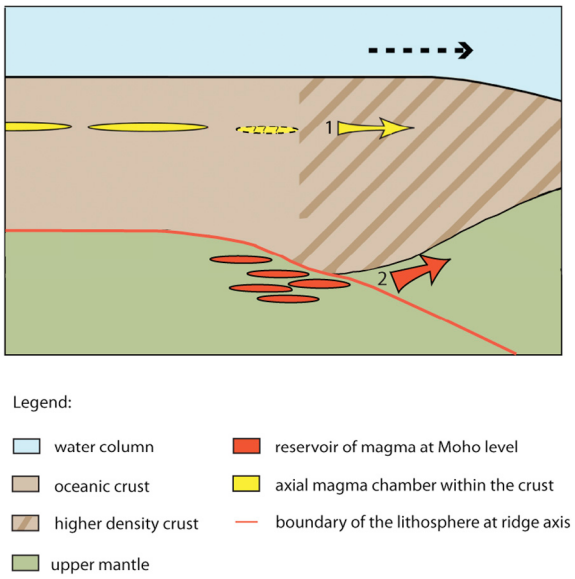

Figure 14. Schematic illustration along the axis of a propagating ridge, summarizing results from our gravity and seismic data analysis. Higher-density crust is found within the propagating ridge tip region and is attributed to the presence of FeTi enriched crustal rocks. High extents of fractionation to form FeTi enriched magmas may occur within magma lenses located within the crust (1) and/or beneath the crust (2) with lateral delivery of magma to the propagating ridge tip.

[41] The presence of wehrlite within the crust, with its high density (~3.3 g/cm^3) and high P wave velocity (8.2 km/s [*Karson et al.*, 1984]), could also contribute to the observed gravity anomalies at the outer pseudofaults. Wehrlite bodies less than 250 m thick have been documented within the Moho Transition Zone of the Oman ophiolite massif [e.g., *Benn and Laurent*, 1987; *Boudier and Nicolas*, 1995; *Koga et al.*, 2001]. At the JdF propagator ridge tips a much thicker wehrlite layer (>1 km thick) with the same lateral extent as the pseudofaults would be necessary to explain both the higher density crust inferred from the gravity modeling as well as the shorter Moho twtt.

7.3. Crustal Thickness Anomalies Adjacent to Pseudofaults

[42] Seismic data indicate the presence of a 10–20 km wide zone of thicker crust (by 350–1300 m, Figures 11 and 12) located up to 10 km from several of the pseudofault crossings and present only on the young crust side of the pseudofaults. Gravity modeling suggests this crust is of possibly higher density (although the inferred density anomalies are small and we cannot rule out over-estimated crustal thicknesses). Observations of modern propagating ridges indicate that seafloor volcanism initiates at comparable distances behind the propagator tip (~10 km) [e.g., *Kleinrock and Hey*, 1989] as the crustal thickness anomaly, and from this coincidence the presence of a local mantle melt excess beneath the magmatic rift tip at propagating ridges is inferred.

[43] Beneath these zones, *Nedimović et al.* [2005] identified bright ridgeward dipping sub-Moho reflection events (locations shown in Figure 12d), which they interpreted as frozen melt sills at the base of the crust emplaced behind the propagating ridge tips. In a 1980s era seismic reflection study located nearby, similar subcrustal reflectors are identified beneath the young crust side of outer pseudofaults OP4 and OP7 [*Calvert et al.*, 1990; *Hasselgren et al.*, 1992]. We interpret the subcrustal events imaged in these regions as the now frozen source magma bodies for the denser, iron-enriched crustal rocks within the pseudofault zones. The formation of highly differentiated FeTi magmas requires presence of magma bodies with low magma replenishment rates and moderate cooling rates to allow closed-system fractionation to occur; such conditions may be common at propagating ridges, as spreading breaks into older and cooler lithosphere [*Sinton et al.*, 1983]. If these melt sills are the source of the more differentiated iron-rich rocks at the propagating ridge tips, lateral melt transport over distances of 10–20 km is required (Figure 14). Lateral transport could occur at sub-Moho depths or by lateral dike intrusion from midcrust lenses that are fed by subcrust lenses below and is presumably enhanced by the local gradients in topography and crustal thickness in the propagating ridge environment.

[44] The best constraints on crustal structure at any propagating offset along the global Mid-Ocean Ridge are from the southward propagating 9°03′N Overlapping Spreading Center (OSC). At this offset, remarkably similar relationships are observed as at the JdF psuedofaults, including an ~20 km wide band of crust that is both thicker and denser, located behind the V-shaped discordant zone left by OSC propagation [*Canales et al.*, 2003; *Singh et al.*, 2006; *Toomey and Hooft*, 2008]. A broad swath of higher crustal magnetizations encompasses the region of thicker and denser crust as well as the bounding V-shaped discordant zone of the OSC [*Carbotte and Macdonald*, 1992]. The highest magnetizations are within the discordant zone coincident with the relict OCS ridge tips, and are attributed to presence of FeTi basalts, which are sampled at the

modern overlap ridges [*Sempere*, 1991]. The similarities in crustal properties at the EPR OSC discordant zone with those inferred for the JdF pseudofaults, including presence of thicker and denser crust behind the propagating offset and iron-enriched crust within the discordant/pseudofault zone, suggest a common origin linked to localized excess melt trapped behind propagating ridge tips.

[45] These local melt anomalies could reflect damming and accumulation of melts at the base of the crust due to pronounced lateral gradients in axial thermal structure behind propagating rift tips. The topography of the base of the lithosphere at a propagating ridge tip is expected to be strongly three dimensional, which may result in accumulation of melts behind the narrowing V-shaped wedge of the lithosphere. Many presently active propagating ridges are moving away from mantle hot spots and the influence of hot spots on ridge axis melt distribution has long been invoked in models for ridge propagation although a direct temporal link has not been established [e.g., *Karsten and Delaney*, 1989; *Wilson*, 1993]. Perhaps mantle melt anomalies at a range of scales (e.g., the Cobb and Heckle) contribute to initiation of propagation, but are not required for propagation to persist, as excess melt accumulations develop behind propagating ridge tips due to the local 3-D structure and contribute to further propagation.

8. Conclusions

[46] Gravity models, in combination with MCS data, corroborate the presence of thicker crust underlying the broad axis-centered plateau found at the Endeavor and Cleft segments which *Carbotte et al.* [2008] attribute to the recent ridge capture of nearby seamount melt anomalies. At all three segments, density variations predicted from plate cooling cannot fully account for the broad axial gravity anomalies and the presence of additional low densities/high temperatures in the mantle below the axis is required. From the width of the axial residual gravity anomaly low, the region of low-density mantle is broader at the Cleft segment and extends beneath both ridge flanks. This is consistent with other indicators of an anomalously warm subaxial regime, compared with elsewhere along the ridge and inconsistent with a significant cold edge effect due to the nearby large age offset Blanco TF.

[47] Gravity and seismic data support the presence of thinner (~0.5 km) crust at the inner and outer pseudofaults and denser crust at outer pseudofaults. Immediately adjacent to the pseudofaults, thicker and possibly denser crust is present, underlain by bright sub-Moho reflections interpreted as frozen magma lenses by *Nedimović et al.* [2005]. We attribute the higher density of the pseudofault zone crust to iron enrichment, resulting from enhanced differentiation of magmas within these nearby subcrustal magma lenses. The bands of thicker crust that directly overlie these subcrust lenses indicate that local melt anomalies are present behind the propagator tips. Excess melt in this region, where stresses resisting propagation will inhibit crack opening, may result in the moderate cooling rates and longer magma residence times needed to generate the more fractionated compositions typical of propagating ridge tips.

Acknowledgments

[48] We thank the reviewers, whose comments greatly improved the paper. We are grateful to M. Studinger for his generous help with GMSYS software and to J. Cochran for discussions regarding aspects of the gravity data modeling. This work was supported by the National Science Foundation grants OCE-0648303 to Lamont-Doherty Earth Observatory, OCE-0648923 to Woods Hole Oceanographic Institution.

References

Benn, K., and R. Laurent (1987), Intrusive suite documented in the Troodos ophiolite plutonic complex, Cyprus, *Geology*, *15*, 821–824, doi:10.1130/0091-7613(1987)15<821:ISDITT>2.0.CO;2.

Boudier, F., and A. Nicolas (1995), Nature of the Moho transition zone in the Oman ophiolite, *J. Petrol.*, *36*, 777–796.

Calvert, A. J., E. A. Hasselgren, and R. M. Clowes (1990), Oceanic rift propagation–a cause of crustal underplating and seamount volcanism, *Geology*, *18*, 886–889, doi:10.1130/0091-7613(1990)018<0886:ORPACO>2.3.CO;2.

Canales, J. P., G. Ito, R. S. Detrick, and J. Sinton (2002), Crustal thickness along the western Galápagos Spreading Center and the compensation of the Galápagos hotspot swell, *Earth Planet. Sci. Lett.*, *203*(1), 311–327, doi:10.1016/S0012-821X(02)00843-9.

Canales, J. P., R. S. Detrick, D. R. Toomey, and W. S. D. Wilcock (2003), Segment-scale variations in the crustal structure of 150–300 kyr old fast spreading oceanic crust (East Pacific Rise, 8°15′N–10°15′N) from wide-angle seismic refraction profiles, *Geophys. J. Int.*, *152*, 766–794, doi:10.1046/j.1365-246X.2003.01885.x.

Canales, J. P., R. S. Detrick, S. M. Carbotte, G. M. Kent, J. B. Diebold, A. Harding, J. Babcock, M. R. Nedimović, and E. van Ark (2005), Upper crustal structure and axial topography at intermediate spreading ridges: Seismic constraints from the southern Juan de Fuca Ridge, *J. Geophys. Res.*, *110*, B12104, doi:10.1029/2005JB003630.

Canales, J. P., M. R. Nedimović, G. M. Kent, S. M. Carbotte, and R. S. Detrick (2009), Seismic reflection images of a

near-axis melt sill within the lower crust at the Juan de Fuca Ridge, *Nature*, *460*(7251), 89–93, doi:10.1038/nature08095.

Carbotte, S. M., and K. Macdonald (1992), East Pacific Rise 8°–10°30′N: Evolution of ridge segments and discontinuities from SeaMARK II and three-dimensional magnetic studies, *J. Geophys. Res.*, *97*, 6959–6982, doi:10.1029/91JB03065.

Carbotte, S. M., R. S. Detrick, A. Harding, J. P. Canales, J. Babcock, G. Kent, E. van Ark, M. R. Nedimović, and J. Diebold (2006), Rift topography linked to magmatism at the intermediate spreading Juan de Fuca Ridge, *Geology*, *34*(3), 209–212, doi:10.1130/G21969.1.

Carbotte, S. M., M. R. Nedimović, J. P. Canales, G. Kent, A. Harding, and M. Marjanović (2008), Variable crustal structure along the Juan de Fuca Ridge: Influence of on-axis hot spots and absolute plate motions, *Geochem. Geophys. Geosyst.*, *9*, Q08001, doi:10.1029/2007GC001922.

Carlson, R. L., and C. N. Herrick (1990), Densities and porosities in the oceanic crust and their variations with depth and age, *J. Geophys. Res.*, *95*, 9153–9170, doi:10.1029/JB095iB06p09153.

Chadwick, J., M. Perfit, I. Ridley, I. Jonasson, G. Kamenov, W. Chadwick, R. Embley, P. le Roux, and M. Smith (2005), Magmatic effects of the Cobb hot spot on the Juan de Fuca Ridge, *J. Geophys. Res.*, *110*, B03101, doi:10.1029/2003JB002767.

Christeson, G. L., J. A. Karson, and K. D. McIntosh (2010), Mapping of seismic layer 2A/2B boundary above the sheeted dike unit at intermediate spreading crust exposed near the Blanco Transform, *Geochem. Geophys. Geosyst.*, *11*, Q03015, doi:10.1029/2009GC002864.

Cochran, J. R., D. J. Fornari, B. J. Coakley, R. Herr, and M. A. Tivey (1999), Continuous near-bottom gravity measurements made with BGM-3 gravimeter in DSV *Alvin* on the East Pacific Rise crest near 9°31′N and 9°50′N, *J. Geophys. Res.*, *104*, 10,841–10,861, doi:10.1029/1999JB900049.

Cormier, M. H., K. Macdonald, and D. Wilson (1995), A three-dimensional gravity analysis of the East Pacific Rise from 18° to 21°30′S, *J. Geophys. Res.*, *100*, 8063–8082, doi:10.1029/95JB00243.

Darbyshire, F. A., R. S. White, and K. F. Priestley (2000), Structure of the crust and uppermost mantle of Iceland from a combined seismic and gravity study, *Earth Planet. Sci. Lett.*, *181*, 409–428, doi:10.1016/S0012-821X(00)00206-5.

Davis, E. E., and J. L. Karsten (1986), On the cause of the asymmetric distribution of seamounts about the Juan de Fuca ridge: Ridge-crest migration over a heterogeneous asthenosphere, *Earth Planet. Sci. Lett.*, *79*, 385–396, doi:10.1016/0012-821X(86)90194-9.

Davis, E. E., A. T. Fisher, J. V. Firth, and the Shipboard Scientific Party (1997), *Proceedings of the Ocean Drilling Program*, *Initial Reports*, vol. 168, 470 pp., Ocean Drill. Program, College Station, Tex.

Desonie, D. L., and R. A. Duncan (1990), The Cobb-Eickelberg seamount chain: Hotspot volcanism with mid-ocean ridge basalt affinity, *J. Geophys. Res.*, *95*, 12,697–12,711, doi:10.1029/JB095iB08p12697.

Detrick, R. S., J. M. Sinton, G. Ito, J. P. Canales, M. Behn, T. Blacic, B. Cushman, J. E. Dixon, D. W. Graham, and J. J. Mahoney (2002), Correlated geophysical, geochemical and volcanological manifestations of plume-ridge interaction along the Galápagos Spreading Center, *Geochem. Geophys. Geosyst.*, *3*(10), 8501, doi:10.1029/2002GC000350.

Embley, R. W., K. M. Murphy, and C. G. Fox (1990), High-resolution studies of the summit of Axial Volcano, *J. Geophys. Res.*, *95*, 12,785–12,812, doi:10.1029/JB095iB08p12785.

Eysteinsson, H., and K. Gunnarsson (1995), Maps of gravity, bathymetry and magnetics for Iceland and surroundings, *Rep. OS-95055/JHD-07*, 39 pp., Orkustofnun, Reykjavik.

Gilbert, L. A., R. E. McDuff, and H. P. Johnson (2007), Porosity of the upper edifice of Axial Seamount, *Geology*, *35*(1), 49–52. (Correction, *Geology, 35*(4), 384.)

Gregg, P. M., J. Lin, M. D. Behn, and L. G. J. Montési (2007), Spreading rate dependence of the gravity structure of oceanic transform faults, *Nature*, *448*, 183–187, doi:10.1038/nature05962.

Hasselgren, E., R. M. Clowes, and A. J. Calvert (1992), Propagating rift pseudofaults—Zones of crustal underplating imaged by multichannel seismic reflection data, *Geophys. Res. Lett.*, *19*, 485–488, doi:10.1029/92GL00368.

Hey, R., and P. Vogt (1977), Spreading centers jumps and sub-axial astenosphere flow near the Galapagos hotspot, *Tectonophysics*, *37*, 41–52, doi:10.1016/0040-1951(77)90038-5.

Hey, R., F. K. Duennebier, and W. J. Morgan (1980), Propagating rifts on midocean ridges, *J. Geophys. Res.*, *85*, 3647–3658, doi:10.1029/JB085iB07p03647.

Hey, R. N., et al. (1992), ALVIN investigation of an active propagating rift system, Galapagos 95.5°W, *Mar. Geophys. Res.*, *14*, 207–226, doi:10.1007/BF01270630.

Hooft, E. E. E., and S. R. Detrick (1995), Relationship between axial morphology, crustal thickness, and mantle temperature along the Juan de Fuca and Gorda Ridges, *J. Geophys. Res.*, *100*, 22,499–22,508, doi:10.1029/95JB02502.

Hooft, E. E. E., M. C. Kleinrock, and C. Ruppel (1995), Rifting of oceanic crust at Endeavor Deep on the Juan Fernandez Microplate, *Mar. Geophys. Res.*, *17*, 251–273, doi:10.1007/BF01203465.

Hooft, E. E. E., B. Brandsdottir, R. Mjelde, H. Shimamura, and Y. Murai (2006), Asymmetric plume-ridge interaction around Iceland: The Kolbeinsey Ridge Iceland Seismic Experiment, *Geochem. Geophys. Geosyst.*, *7*, Q05015, doi:10.1029/2005GC001123.

Ito, G., and J. Lin (1995), Mantle temperature anomalies along the past and paleoaxes of the Galpagos spreading center as inferred from gravity analyses, *J. Geophys. Res.*, *100*, 3733–3745, doi:10.1029/94JB02594.

Ito, G., J. Lin, and D. Grahma (2003), Observational and theoretical studies of the dynamics of mantle plume–mid-ocean ridge interaction, *Rev. Geophys.*, *41*(4), 1017, doi:10.1029/2002RG000117.

Iturrino, G. J., N. I. Christensen, S. Kirby, and M. H. Salisbury (1991), Seismic velocities and elastic properties of oceanic gabbroic rocks from Hole 735B, *Proc. Ocean Drill. Program Sci. Results*, *118*, 227–244.

Johnson, H. P., J. L. Karsten, J. R. Delaney, E. E. Davis, R. G. Currie, and R. L. Chase (1983), A detailed study of the Cobb offset of the Juan de Fuca Ridge: Evolution of a propagating rift, *J. Geophys. Res.*, *88*, 2297–2315, doi:10.1029/JB088iB03p02297.

Karato, S., and K. Becker (1983), Physical properties of sediments from the Galapagos region and their implications for hydrothermal convection, *Initial Rep. Deep Sea Drill. Proj.*, *70*, 355–368.

Karson, J. A., J. A. Collins, and J. F. Casey (1984), Geologic and seismic velocity structure of the crust/mantle transition in the Bay of Islands ophiolite complex, *J. Geophys. Res.*, *89*, 6126–6138, doi:10.1029/JB089iB07p06126.

Karsten, L. J., and R. J. Delaney (1989), Hotspot-Ridge crest convergence in the Northeast Pacific, *J. Geophys. Res.*, *94*, 700–712, doi:10.1029/JB094iB01p00700.

Klein, E., C. Langmuir, and H. Staudigel (1991), Geochemistry of basalts from the Southeast Indian Ridge, 115°E–138°E, *J. Geophys. Res.*, *96*, 2089–2107, doi:10.1029/90JB01384.

Kleinrock, M. C., and R. N. Hey (1989), Detailed tectonics near the tip of the Galapagos 95.5°W propagator: How the lithosphere tears and a spreading axis develops, *J. Geophys. Res.*, *94*, 13,801–13,838, doi:10.1029/JB094iB10p13801.

Koga, K. T., P. B. Kelemen, and N. Shimizu (2001), Petrogenesis of the crust-mantle transition zone and the origin of lower crustal wehrlite in the Oman ophiolite, *Geochem. Geophys. Geosyst.*, *2*, 1038, doi:10.1029/2000GC000132.

Kruse, E. S., S. F. Tebbens, D. F. Naar, Q. Lou, and R. Bird (2000), Comparisons of gravity anomalies at pseudofaults, fracture zones, and nontransform discontinuities from fast to slow spreading areas, *J. Geophys. Res.*, *105*, 28,399–28,410, doi:10.1029/2000JB900281.

Marescotti, P., D. A. Vanko, and R. Cabella (2000), From oxidizing to reducing alteration: Mineralogical variations in pillow basalts from the east flank, Juan de Fuca Ridge, *Proc. Ocean Drill. Program Sci. Results*, *168*, 119–136.

Martinez, F., D. F. Naar, T. B. Reed, and R. N. Hey (1991), Three-dimensional SeaMARC II, gravity and magnetics study of large offset rift propagation at the Pito Rift, Easter microplate, *Mar. Geophys. Res.*, *101*, 13,715–13,730.

Nedimović, M. R., S. M. Carbotte, A. J. Harding, R. S. Detrick, J. P. Canales, J. B. Diebold, G. M. Kent, M. Tischer, and J. M. Babcock (2005), Frozen magma lenses below the oceanic crust, *Nature*, *436*, 1149–1152, doi:10.1038/nature03944.

Nedimović, M. R., S. M. Carbotte, J. B. Diebold, A. J. Harding, J. P. Canales, and G. M. Kent (2008), Upper crustal evolution across the Juan de Fuca ridge flanks, *Geochem. Geophys. Geosyst.*, *9*, Q09006, doi:10.1029/2008GC002085.

Phipps Morgan, J., and E. M. Parmentier (1985), Causes and rate-limiting mechanism of ridge propagation: A Fracture Mechanism Model, *J. Geophys. Res.*, *90*, 8603–8612, doi:10.1029/JB090iB10p08603.

Schilling, J. G., R. H. Kingsley, and J. D. Devine (1982), Galapagos hot-spot spreading center system: Spatial petrological and geochemical variations (83°W–101°W), *J. Geophys. Res.*, *87*, 5593–5610, doi:10.1029/JB087iB07p05593.

Sempere, J. C. (1991), High magnetization zones near spreading center discontinuities, *Earth Planet. Sci. Lett.*, *107*, 389–405, doi:10.1016/0012-821X(91)90085-V.

Singh, S. C., et al. (2006), Seismic reflection images of the Moho underlying melt sills at the East Pacific Rise, *Nature*, *442*, 287–290, doi:10.1038/nature04939.

Sinton, J. M., D. S. Wilson, D. M. Christie, R. N. Hey, and J. R. Delaney (1983), Petrologic consequences of rift propagation on oceanic spreading ridges, *Earth Planet. Sci. Lett.*, *62*, 193–207, doi:10.1016/0012-821X(83)90083-3.

Talwani, M., L. J. Worzel, and M. Landisman (1959), Rapid gravity computations for two-dimensional bodies with application to the Mendocino Submarine Fracture Zone, *J. Geophys. Res.*, *64*, 49–59, doi:10.1029/JZ064i001p00049.

Tivey, M. A., and H. P. Johnson (1990), The magnetic structure of Axial Seamount: Juan de Fuca Ridge, *J. Geophys. Res.*, *95*, 12,735–12,750, doi:10.1029/JB095iB08p12735.

Toomey, D. R., and E. E. E. Hooft (2008), Mantle upwelling, magmatic differentiation, and the meaning of axial depth at fast-spreading ridges, *Geology*, *36*, 679–682, doi:10.1130/G24834A.1.

Turcotte, D., and J. Schubert (2002), *Geodynamics*, 2nd ed., Cambridge Univ. Press, New York.

Van Avendonk, H. J. A., A. J. Harding, J. A. Orcutt, and J. S. McClain (1998), A two-dimensional tomographic study of the Clipperton transform fault, *J. Geophys. Res.*, *103*, 17,885–17,899, doi:10.1029/98JB00904.

West, B. P., J. Lin, and D. M. Christie (1999), Forces driving ridge propagation, *J. Geophys. Res.*, *104*, 22,845–22,858, doi:10.1029/1999JB900154.

West, M., W. Menke, and M. Tolstoy (2003), Focused magma supply at the intersection of the Cobb hotspot and the Juan de Fuca ridge, *Geophys. Res. Lett.*, *30*(14), 1724, doi:10.1029/2003GL017104.

Wilson, D. S. (1992), Focused mantle upwelling beneath mid-ocean ridges: Evidence from seamount formation and isostatic compensation of topography, *Earth Planet. Sci. Lett.*, *113*, 41–55, doi:10.1016/0012-821X(92)90210-M.

Wilson, D. S. (1993), Confidence intervals for motion and deformation of the Juan de Fuca plate, *J. Geophys. Res.*, *98*, 16,053–16,071, doi:10.1029/93JB01227.

Wilson, D. S., R. N. Hey, and C. Nishimura (1984), Propagation as a mechanism of reorientation of the Juan de Fuca Ridge, *J. Geophys. Res.*, *89*, 9215–9225, doi:10.1029/JB089iB11p09215.

Won, I. J., and M. Bevis (1987), Computing the gravitational and magnetic anomalies due to a polygon: Algorithms and Fortran subroutines, *Geophysics*, *52*, 232–238, doi:10.1190/1.1442298.